


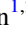








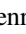


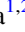





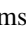

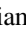




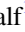
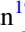

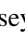


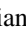







TOI-3714 b and TOI-3629 b: Two Gas Giants Transiting M Dwarfs Confirmed with the Habitable-zone Planet Finder and NEID

Caleb I. Cañas^{1,2,25} , Shubham Kanodia^{1,2} , Chad F. Bender³ , Suvrath Mahadevan^{1,2} , Gudmundur Stefánsson^{4,26} , William D. Cochran⁵ , Andrea S. J. Lin^{1,2} , Hsiang-Chih Hwang⁶ , Luke Powers^{1,2} , Andrew Monson¹ , Elizabeth M. Green³ , Brock A. Parker⁷ , Tera N. Swaby⁷ , Henry A. Kobulnicky⁷ , John Wisniewski⁸ , Arvind F. Gupta^{1,2} , Mark E. Everett⁹ , Sinclaire Jones⁴ , Benjamin Anjakos¹⁰ , Corey Beard¹¹ , Cullen H. Blake¹² , Scott A. Diddams^{13,14} , Zehao Dong (董泽浩)¹⁰, Connor Fredrick^{14,15} , Elnaz Hakemiamjad¹⁰ , Leslie Hebb¹⁶ , Jessica E. Libby-Roberts^{1,2} , Sarah E. Logsdon⁹ , Michael W. McElwain¹⁷ , Andrew J. Metcalf^{13,14,18} , Joe P. Ninan¹⁹ , Jayadev Rajagopal⁹ , Lawrence W. Ramsey^{1,2} , Paul Robertson¹¹ , Arpita Roy^{20,21} , Jacob Ruhle¹⁰ , Christian Schwab²² , Ryan C. Terrien²³ , and Jason T. Wright^{1,2,24} 

¹ Department of Astronomy & Astrophysics, The Pennsylvania State University, 525 Davey Laboratory, University Park, PA 16802, USA; canas@psu.edu

² Center for Exoplanets and Habitable Worlds, The Pennsylvania State University, 525 Davey Laboratory, University Park, PA 16802, USA

³ Steward Observatory, The University of Arizona, 933 N. Cherry Avenue, Tucson, AZ 85721, USA

⁴ Department of Astrophysical Sciences, Princeton University, 4 Ivy Lane, Princeton, NJ 08540, USA

⁵ McDonald Observatory and Center for Planetary Systems Habitability, The University of Texas at Austin, Austin, TX 78730, USA

⁶ School of Natural Sciences, Institute for Advanced Study, Princeton, 1 Einstein Drive, NJ 08540, USA

⁷ Department of Physics & Astronomy, University of Wyoming, Laramie, WY 82070, USA

⁸ Homer L. Dodge Department of Physics and Astronomy, University of Oklahoma, 440 W. Brooks Street, Norman, OK 73019, USA

⁹ NSF's National Optical-Infrared Astronomy Research Laboratory, 950 N. Cherry Avenue, Tucson, AZ 85719, USA

¹⁰ Department of Astronomy, The University of Arizona, 933 N. Cherry Avenue, Tucson, AZ 85721, USA

¹¹ Department of Physics & Astronomy, The University of California, Irvine, Irvine, CA 92697, USA

¹² Department of Physics and Astronomy, University of Pennsylvania, 209 South 33rd Street, Philadelphia, PA 19104 USA

¹³ Time and Frequency Division, National Institute of Standards and Technology, 325 Broadway, Boulder, CO 80305, USA

¹⁴ Department of Physics, University of Colorado, 2000 Colorado Avenue, Boulder, CO 80309, USA

¹⁵ Associate of the National Institute of Standards and Technology, 325 Broadway, Boulder, CO 80305, USA

¹⁶ Department of Physics, Hobart and William Smith Colleges, 300 Pulteney Street, Geneva, NY 14456, USA

¹⁷ Exoplanets and Stellar Astrophysics Laboratory, NASA Goddard Space Flight Center, Greenbelt, MD 20771, USA

¹⁸ Space Vehicles Directorate, Air Force Research Laboratory, 3550 Aberdeen Ave. SE, Kirtland AFB, NM 87117, USA

¹⁹ Department of Astronomy and Astrophysics, Tata Institute of Fundamental Research, Homi Bhabha Road, Colaba, Mumbai 400005, India

²⁰ Space Telescope Science Institute, 3700 San Martin Drive, Baltimore, MD 21218, USA

²¹ Department of Physics and Astronomy, Johns Hopkins University, 3400 N Charles Street, Baltimore, MD 21218, USA

²² Department of Physics and Astronomy, Macquarie University, Balaclava Road, North Ryde, NSW 2109, Australia

²³ Department of Physics and Astronomy, Carleton College, One North College Street, Northfield, MN 55057, USA

²⁴ Penn State Extraterrestrial Intelligence Center, 525 Davey Laboratory, The Pennsylvania State University, University Park, PA, 16802, USA

Received 2022 January 24; revised 2022 May 19; accepted 2022 June 11; published 2022 July 14

Abstract

We confirm the planetary nature of two gas giants discovered by the Transiting Exoplanet Survey Satellite to transit M dwarfs. TOI-3714 ($V = 15.24$, $J = 11.74$) is an M2 dwarf hosting a hot Jupiter ($M_p = 0.70 \pm 0.03 M_J$ and $R_p = 1.01 \pm 0.03 R_J$) on an orbital period of 2.154849 ± 0.000001 days with a resolved white dwarf companion. TOI-3629 ($V = 14.63$, $J = 11.42$) is an M1 dwarf hosting a hot Jupiter ($M_p = 0.26 \pm 0.02 M_J$ and $R_p = 0.74 \pm 0.02 R_J$) on an orbital period of $3.936551^{+0.000005}_{-0.000006}$ days. We characterize each transiting companion using a combination of ground-based and space-based photometry, speckle imaging, and high-precision velocimetry from the Habitable-zone Planet Finder and the NEID spectrographs. With the discovery of these two systems, there are now nine M dwarfs known to host transiting hot Jupiters. Among this population, TOI-3714 b ($T_{\text{eq}} = 750 \pm 20$ K and $\text{TSM} = 98 \pm 7$) and TOI-3629 b ($T_{\text{eq}} = 690 \pm 20$ K and $\text{TSM} = 80 \pm 9$) are warm gas giants amenable to additional characterization with transmission spectroscopy to probe atmospheric chemistry and, for TOI-3714, obliquity measurements to probe formation scenarios.

Unified Astronomy Thesaurus concepts: Exoplanet systems (484); Extrasolar gaseous giant planets (509)

1. Introduction

Short-period ($P < 10$ days) Jupiter-sized ($R_p \geq 8 R_{\oplus}$) exoplanets, or hot Jupiters, are rare in the galaxy. Results from radial

velocity (RV) surveys (e.g., Cumming et al. 2008; Mayor et al. 2011; Wright et al. 2012), ground-based photometry surveys (e.g., Obermeier et al. 2016), and space-based surveys (Howard et al. 2012; Petigura et al. 2018; Zhou et al. 2019) have determined the occurrence rate for hot Jupiters orbiting Sun-like (FGK) dwarfs to be $\lesssim 1\%$. Despite the fact that over 400 hot Jupiters have been detected orbiting Sun-like stars, there is no consensus as to the origin mechanisms required to create this population of exoplanets (see Dawson & Johnson 2018). Many hypotheses have been proposed to explain the origin of these planets, including star-planet interactions (e.g., Wu & Murray 2003; Petrovich 2015a),

²⁵ NASA Earth and Space Science Fellow.

²⁶ Henry Norris Russell Fellow.

planet–planet interactions (e.g., Naoz et al. 2011), migration due to planet–disk interactions (e.g., Lin et al. 1996), high-eccentricity migration (e.g., Rasio & Ford 1996; Weidenschilling & Marzari 1996; Ford & Rasio 2008; Petrovich 2015b), and in-situ formation (e.g., Batygin et al. 2016; Boley et al. 2016).

From analysis of the Kepler field (e.g., Dressing & Charbonneau 2015; Mulders et al. 2015; Hardegree-Ullman et al. 2019; Hsu et al. 2020), the occurrence rate of small ($1 R_{\oplus} < R_p < 4 R_{\oplus}$) planets on short-period ($P < 200$ days) orbits is larger for M dwarfs, the most abundant type of star in the galaxy (Henry et al. 2018), compared to Sun-like stars. The occurrence rate of these small planets also increases for later-type M dwarfs. RV surveys have similarly revealed the abundance of low-mass planets ($1 M_{\oplus} < M_p < 10 M_{\oplus}$) on short-period orbits ($P < 200$ days) as companions to M dwarfs (e.g., Bonfils et al. 2013; Tuomi et al. 2014, 2019; Sabotta et al. 2021). Jupiter-like planets, however, are expected to be rare companions to M dwarfs under the theory of core accretion (e.g., Laughlin et al. 2004; Ida & Lin 2005; Kennedy & Kenyon 2008). In the core accretion model, a gas giant planet forms from a runaway process resulting in the rapid accretion of gas onto a planetary core (e.g., Pollack et al. 1996; Ida & Lin 2004; Hubickyj et al. 2005). This model predicts a small number of gas giants orbiting M dwarfs, because the low surface density of an M dwarf protoplanetary disk would impede the formation of massive cores required for the onset of runaway gas accretion.

To date, M dwarf RV surveys (e.g., Endl et al. 2006; Bonfils et al. 2013; Tuomi et al. 2019; Sabotta et al. 2021) and photometric surveys (Kovács et al. 2013; Obermeier et al. 2016) have only been able to constrain the occurrence rate to $\lesssim 1\%$ – 2% for hot Jupiters orbiting M dwarfs. Prior to this paper, there were seven hot Jupiters known to transit M dwarfs: Kepler-45 b (Johnson et al. 2012), HATS-6 b (Hartman et al. 2015), NGTS-1 b (Bayliss et al. 2018), HATS-71 b (Bakos et al. 2020), HATS-74A b and HATS-75b (Jordán et al. 2022), and TOI-3757 b (Kanodia et al. 2022).

In this paper, we confirm the planetary nature of two gas giants transiting the M dwarfs TOI-3714 ($V = 14.63$, $J = 11.42$, $T = 12.79$) and TOI-3629 ($V = 15.24$, $J = 11.74$, $T = 13.18$). We characterize each system using space- and ground-based photometry, speckle imaging, and precision RVs obtained with the Habitable-zone Planet Finder (HPF; Mahadevan et al. 2012, 2014) and NEID (Halverson et al. 2016; Schwab et al. 2016) spectrographs. We derive stellar parameters for the host stars using our HPF spectra and use the RVs measured from both HPF and NEID to confirm that each transiting companion is a hot Jupiter.

This paper is structured as follows: Section 2 presents the photometric, imaging, and spectroscopic observations used to characterize each system. The characterization of the host stars and the best estimates of the stellar parameters are described in Section 3. The modeling and analysis of the photometry and RVs are presented in Section 4. Section 5 provides further discussion of the nature of these planets and the feasibility for future study. We end with a summary of our key results in Section 6.

2. Observations

2.1. Transiting Exoplanet Survey Satellite

The Transiting Exoplanet Survey Satellite (TESS; Ricker et al. 2015) observed TOI-3629 (TIC 455784423; Gaia EDR3

2881820324294985856) and TOI-3714 (TIC 155867025; Gaia EDR3 178924390478792320) in long-cadence mode (30 min cadence). TOI-3629 was observed during Sector 17 (2019 October 7 through 2019 November 2) and TOI-3714 was observed during Sector 19 (2019 November 27 through 2019 December 24). Similar to TOI-1899 (Cañas et al. 2020), we identified TIC 455784423.01 as a planetary candidate using a custom pipeline to search for transiting candidates in short- and long-cadence TESS data orbiting M dwarfs that were amenable to RV observations with HPF. At the time when we searched TESS data, the “quick-look pipeline” (QLP) developed by Huang et al. (2020a, 2020b) was releasing candidates from the southern TESS sectors. Our search was not designed for completeness but to identify a few ($\lesssim 10$) M dwarfs with Jupiter-sized transiting companions that were most likely planetary in nature.

Briefly, this pipeline was developed to identify transiting companions to bright (TESS magnitude of $T < 13$) M dwarfs ($T_e < 4000$ K) from the catalog of cool dwarfs (a value of `splists = cooldwarfs_v8`; Muirhead et al. 2018) in the TESS input catalog (TIC; Stassun et al. 2019) that are observable from the Hobby–Eberly Telescope (HET; Ramsey et al. 1994, 1998) at the McDonald Observatory ($-11^\circ < \delta < 71^\circ$). These constraints resulted in an average of ~ 2000 stars to process per sector. Our pipeline uses the `lightkurve` package (Lightkurve Collaboration et al. 2018) to detrend (i) short-cadence light curves provided by the TESS science processing operations center (Jenkins et al. 2016) and (ii) long-cadence derived from calibrated full-frame images using `eleanor` (Feinstein et al. 2019) with a Savitzky–Golay filter. The pipeline searches for transit-like events in the detrended photometry using the box least-squares algorithm (Kovács et al. 2002) and models the transit signal following the formalism from Mandel & Agol (2002) as implemented in the `batman` package (Kreidberg 2015). The transit-like events are vetted for centroid offsets and inconsistencies ($> 3\sigma$ discrepant) with the stellar density recovered by the transit fit (e.g., Seager & Mallén-Ornelas 2003; Winn 2010) and the stellar density reported by TIC. Signals that were identified were subsequently vetted by members of the HPF team before we began RV observations.

We detected one planet candidate with a depth of $\sim 1.5\%$ and a period of ~ 3.94 days. This event was subsequently identified (at a comparable period and depth) by the QLP and given the designation TOI-3629.01. It is one of the planetary candidates from the “faint star search”²⁷, an effort to extend the nominal search and vetting of TESS objects of interests to stars with a TESS magnitude of $T < 13.5$ (Kunimoto et al. 2022). The faint star search also identified TOI-3714.01 as a transiting candidate with a depth of $\sim 4.5\%$ and a period of ~ 2.15 days. This target was excluded from our search due to its faintness ($T = 13.18$).

We extract the photometry from the TESS full-frame images using `eleanor`, which calls the TESScut²⁸ service (Brasseur et al. 2019) to obtain a cutout of 31×31 pixels of the calibrated full-frame images centered on each target. `eleanor` removes the background, corrects for systematics, and derives a light curve for various combinations of apertures when processing a target. The final light curve is the one that minimizes the combined differential photometric precision

²⁷ <https://tess.mit.edu/qlp/>

²⁸ <https://mast.stsci.edu/tesscut/>

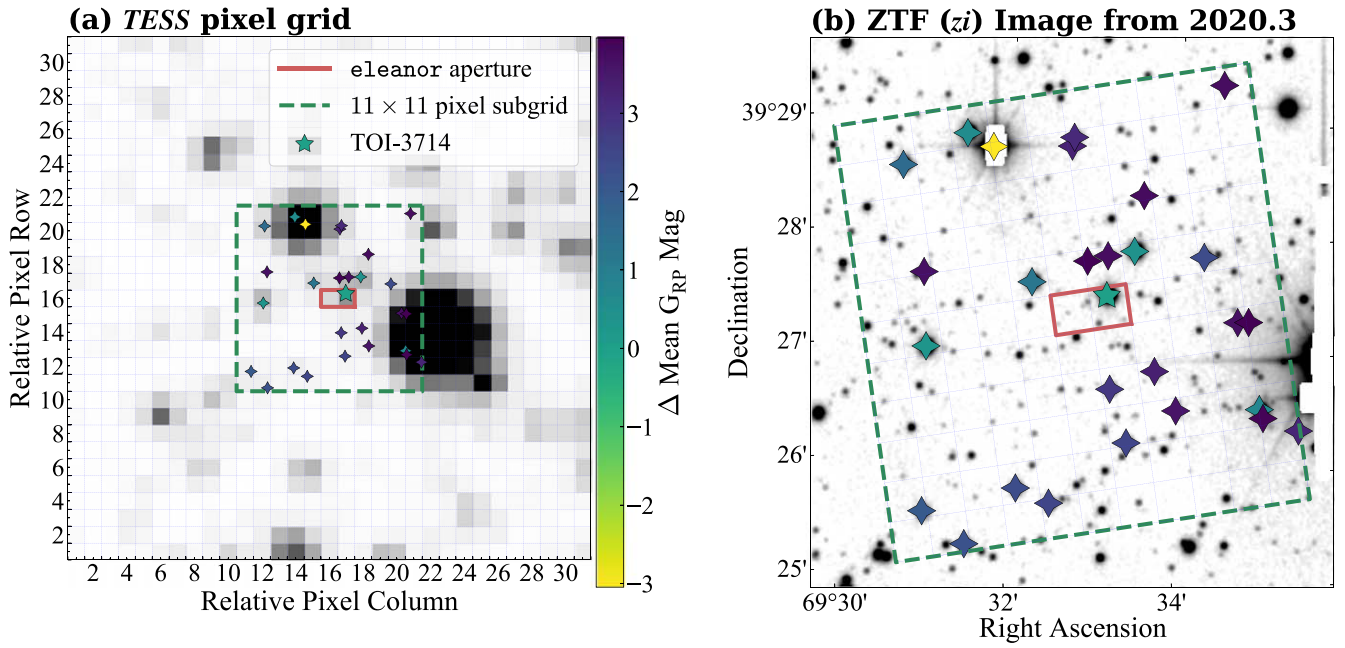


Figure 1. (a) The 31×31 TESS target pixel cutout centered around TOI-3714 (marked as a star). Stars identified in Gaia EDR3 with magnitudes $\Delta G_{RP} < 4$ are marked with diamond stars for reference. Stars with $\Delta G_{RP} < 0$ are brighter than the host star. The dashed line denotes the TESS 11×11 pixel subgrid that is shown in (b). (b) Overlay of the TESS 11×11 pixel subgrid, TOI-3714, and other comparably bright stars on a ZTF *zi* image.

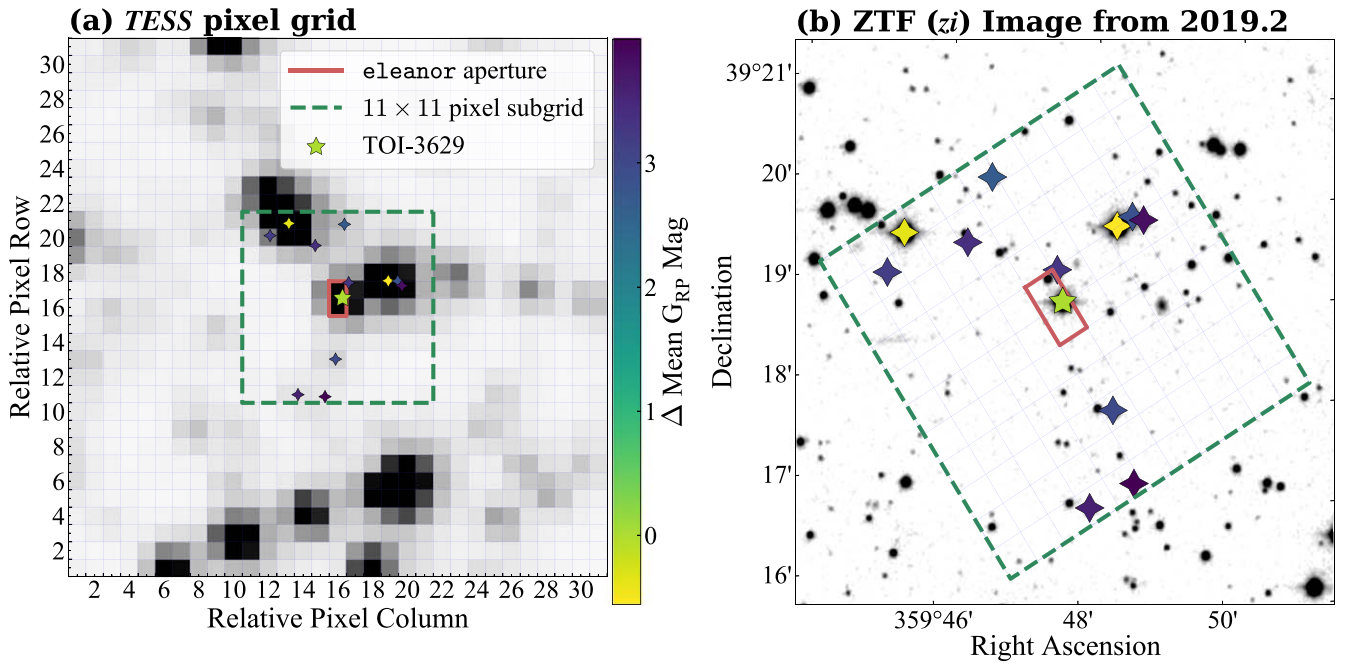


Figure 2. Identical to Figure 1 but for TOI-3629. (a) The 31×31 TESS target pixel cutout centered around TOI-3629 (marked as a star). Stars identified in Gaia EDR3 having magnitudes $\Delta G_{RP} < 4$ are marked with diamond stars. Stars with $\Delta G_{RP} < 0$ are brighter than the host star. (b) Overlay of the TESS 11×11 pixel subgrid, TOI-3629, and other comparably bright stars on a ZTF *zi* image.

(CDPP) after the data are binned to 1 hr timescales. The CDPP was originally defined for Kepler as the rms of the photometric noise on transit timescales (Jenkins et al. 2010). Minimizing this value ensures that sharp features on relatively short timescales, such as transits, are preserved. The final CDPP was 2902 ppm for TOI-3714 and 2219 ppm for TOI-3629.

Figures 1 and 2 show the photometric images for TOI-3629 and TOI-3714, respectively. Panel (a) in both figures presents the TESS full-frame image cutouts and the apertures used to derive the light curves for each target. In panel (b), a smaller

11×11 pixel subgrid of the TESS image and the light curve apertures are overlotted on images from the Zwicky Transient Facility (ZTF; Masci et al. 2019). For each target, the preferred aperture is a 2×1 rectangular aperture centered on the host star. To investigate the impact of background stars as a source of dilution, we searched the 11×11 TESS pixel grid centered on each target in Gaia Early Data Release 3 (EDR3; Gaia Collaboration et al. 2021). Similar to Gandolfi et al. (2018), we use the Gaia G_{RP} bandpass as an approximation to the TESS bandpass. Gaia EDR3 reveals there are no bright stellar

companions in each aperture having $\Delta G_{\text{RP}} < 4$, where ΔG_{RP} is the difference between the G_{RP} magnitude of a star and the respective value for the TOI host star.

The TESS light curves used in this work are the `CORR_FLUX` values calculated by `eleanor`. The corrected flux removes signals correlated with position (x and y pixel position), measured background, and time in the simple aperture flux. Observations where the background is larger than the stellar flux (`FLUX_BKG > CORR_FLUX`) or with nonzero data quality flags (Table 28 in Tenenbaum & Jenkins 2018) are excluded from analysis. Figures 3 and 4 present all photometry, including the TESS light curve, analyzed in this work.

2.2. RBO 0.6 m Telescope

We used the 0.6 m telescope at the Red Buttes Observatory (RBO) in Wyoming (Kasper et al. 2016) to observe (i) TOI-3714 on the nights of 2021 August 16 and 2021 November 19 and (ii) TOI-3629 on the nights of 2021 September 26 and 2021 October 4. The 0.6 m telescope is a $f/8.43$ Ritchey–Chrétien Cassegrain constructed by DFM Engineering, Inc. and equipped with an Apogee Alta F16M camera. The observations on 2021 October 4 of TOI-3629 were obtained in the Bessell V filter (Bessell 1990), while the other observations were obtained in the Bessell I filter. All observations used the 2×2 on-chip binning mode, which has a gain of $1.39 \text{ e}^- / \text{ADU}$, a plate scale of $0''.731 \text{ pixel}^{-1}$, and a readout time of ~ 2.4 s. Each target was defocused moderately and observed using an exposure time of 240 s.

The RBO light curves were derived using `AstroImageJ` (Collins et al. 2017). Following the methodology in Stefánsson et al. (2017), the estimated scintillation noise was included in the flux uncertainty. The final reductions used a photometric aperture radius of 10 pixels ($7''.3$), an inner sky radius of 20 pixels ($14''.6$), and an outer sky radius of 30 pixels ($21''.9$).

2.3. APO 3.5 m Telescope

We used the 3.5 m Astrophysical Research Consortium (ARC) Telescope Imaging Camera (ARCTIC; Huehnerhoff et al. 2016) on the ARC 3.5 m Telescope at Apache Point Observatory (APO) to obtain a transit of TOI-3714 on the night of 2021 November 21. The observations were performed in the Sloan i' filter using an engineered diffuser (Stefánsson et al. 2017) with an exposure time of 45 s. The average seeing for the night was $\sim 1''.0$. ARCTIC was operated in the quad and fast readout modes using the 4×4 on-chip binning mode to achieve a gain of $2 \text{ e}^- / \text{ADU}$, a plate scale of $0''.456 \text{ pixel}^{-1}$, and a readout time of 2.7 s. Similar to the RBO data, we processed the photometry using `AstroImageJ` and included the scintillation noise estimate in the flux uncertainty. The final reduction used a photometric aperture radius of 10 pixels ($4''.6$), an inner sky radius of 20 pixels ($9''.1$), and an outer sky radius of 30 pixels ($13''.7$).

2.4. Kuiper 61" Telescope

We used the 61" (1.55 m) Kuiper Telescope located on Mt. Bigelow, Arizona to observe TOI-3629 on the night of 2021 October 16. The Kuiper Telescope²⁹ is equipped with the Mont4k imager, which uses a 4096×4097 Fairchild CCD486 detector to provide a field of view of $9''.7 \times 9''.7$. TOI-3629 was

observed in the Harris R band using a 30 s exposure time with an average seeing of $\sim 1''.7$. The pixels were binned in 3×3 mode to shorten the readout time. This achieves a plate scale of $0''.42 \text{ pixel}^{-1}$. Similar to the RBO data, we processed the photometry using `AstroImageJ` and included the scintillation noise estimate in the flux uncertainty. The final reduction used a photometric aperture radius of 8 pixels ($3''.6$), an inner sky radius of 14 pixels ($6''.3$), and an outer sky radius of 22 pixels ($9''.9$).

2.5. ZTF Photometry

ZTF data for TOI-3714 and TOI-3629 are publicly available under DR11.³⁰ Both objects were observed through a public program designed to observe TESS northern sectors by ZTF (van Roestel et al. 2019). ZTF has a plate scale of $1''.012 \text{ pixel}^{-1}$ (Yao et al. 2019) and the exposures for all observations are 30 s long. We follow the advice of the ZTF Science Data System Explanatory Supplement³¹ (ZDS) and reject bad-quality data with (i) nonzero `catflag` values (see Section 13.6 in ZDS), (ii) values of $\chi \geq 4$, where χ is the rms of the residuals to the PSF fit on the source performed by the ZTF pipeline, and (iii) values of $|\text{sharp}| \geq 0.5$, where `sharp` is the difference of the observed and model squared PSF FWHM. TOI-3714 has (i) 512 observations spanning 2018 April 08 through 2022 March 2 with a median cadence of 1 day and a median precision of $\sim 1.3\%$ in the zr filter and (ii) 355 observations spanning 2018 March 29 through 2022 March 2 with a median cadence of 2 days and a median precision of $\sim 1.7\%$ in the zg filter. TOI-3629 has (i) 695 observations spanning 2018 May 18 through 2022 February 18 with a median cadence of 1 day and a median precision of $\sim 1.0\%$ in the zr filter and (ii) 574 observations spanning 2018 May 25 through 2022 February 18 with a median cadence of 1 day and a median precision of $\sim 1.1\%$ in the zg filter.

2.6. High-contrast Imaging

TOI-3629 and TOI-3714 were observed on 2021 October 25 and 2021 December 21, respectively, using the speckle imaging instrument NESSI (Scott et al. 2018) on the WIYN 3.5 m Telescope at Kitt Peak National Observatory (KPNO). Due to the faintness of these targets ($r' > 14$), the images were acquired in Sloan r' (TOI-3629 only) and z' instead of the narrower filters that NESSI traditionally uses. TOI-3714 was observed only in the Sloan z' filter because hardware issues during the observing run allowed for operations only with the redder filter. The images in each filter were reconstructed following the procedures outlined in Howell et al. (2011).

TOI-3629 was also observed as part of the Robo-AO Kepler M dwarf multiplicity survey (Lamman et al. 2020) on 2016 October 19. The observations were performed using the Robo-AO laser adaptive optics system (Baranec et al. 2013, 2014) on the 2.1 m telescope at KPNO (Jensen-Clem et al. 2018) using a 1.85 m circular aperture mask on the primary mirror. These observations were taken in the Sloan i' filter. Lamman et al. (2020) have made the Robo-AO contrast curve for TOI-3629 publicly available on the Exoplanet Follow-up Observing Program TESS website.³² The Robo-AO observation reveals

³⁰ <https://www.ztf.caltech.edu/ztf-public-releases.html>

³¹ https://web.ipac.caltech.edu/staff/fmasci/ztf/ztf_pipelines_deliverables.pdf

³² https://exofop.ipac.caltech.edu/tess/view_tag.php?tag=13940

²⁹ <http://james.as.arizona.edu/~psmith/61inch/CCD/basicinfo.html>

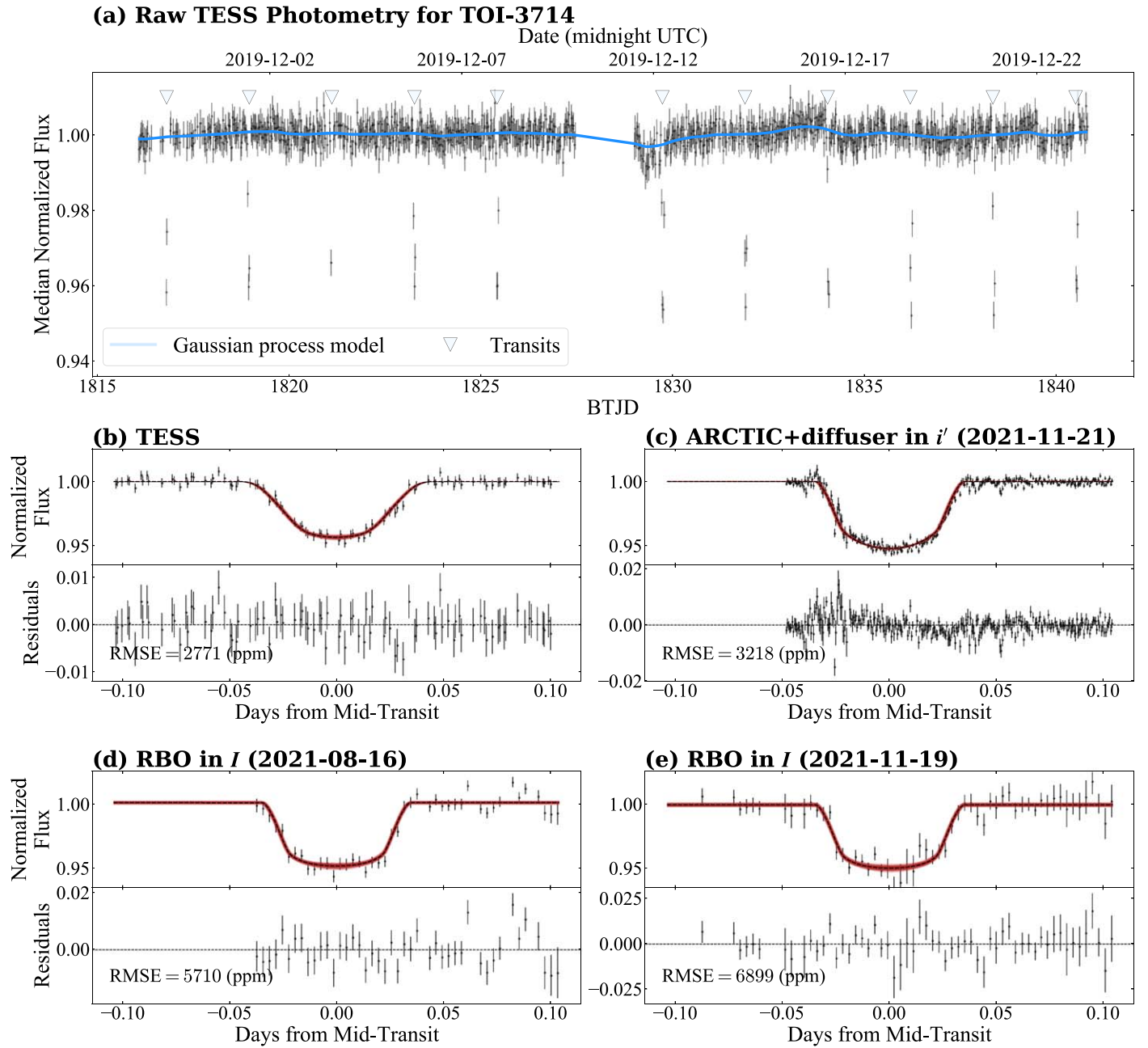


Figure 3. (a) Median normalized TESS light curve for TOI-3714 derived with `eleonor`. The solid blue line is the best-fitting Gaussian process model used to detrend the light curve. The mid-transit times are indicated by the triangles. (b)–(e) Light curves for TESS, ARCTIC, and RBO. In (b)–(e), the best-fitting model from the joint fit to the photometry and RVs is plotted as a dashed line while the shaded regions denote the 1σ (darkest), 2σ , and 3σ (lightest) extent of the model posteriors. The modeling of the photometry and RVs is described in detail in Section 4.

no bright ($\Delta\text{mag} < 4$) stellar companions at separations of $0''.75$ – $1''.75$ from TOI-3629.

Figures 5 and 6 show the 5σ contrast curves for TOI-3629 and TOI-3714, respectively, along with an inset of the NESSI speckle image in the z' filter. Together, the NESSI and Robo-AO data show there are no bright ($\Delta\text{mag} < 4$) companions and no significant source of dilution at separations of $0''.2$ – $1''.2$ from either target.

2.7. HPF Spectrograph

HPF is a high-resolution ($R \sim 55,000$), fiber-fed (Kanodia et al. 2018), temperature controlled (Stefánsson et al. 2016),

near-infrared ($\lambda \sim 8080$ – 12780 Å) spectrograph located on the 10 m HET at the McDonald Observatory in Texas (Mahadevan et al. 2012, 2014). Observations are executed in a queue by the HET resident astronomers (Shetrone et al. 2007). Between 2021 January 18 and 2022 January 14, we obtained 12 visits of TOI-3714 and 23 visits of TOI-3629. The median signal-to-noise ratios (S/N) per 1D extracted pixel at 1070 nm are 44 and 54, respectively, for these targets.

The `HxRgproc` tool³³ (Ninan et al. 2018) was used to process the raw HPF data and perform bias noise removal, nonlinearity correction, cosmic-ray correction, and slope/flux

³³ <https://github.com/indiajoe/HxRgproc>

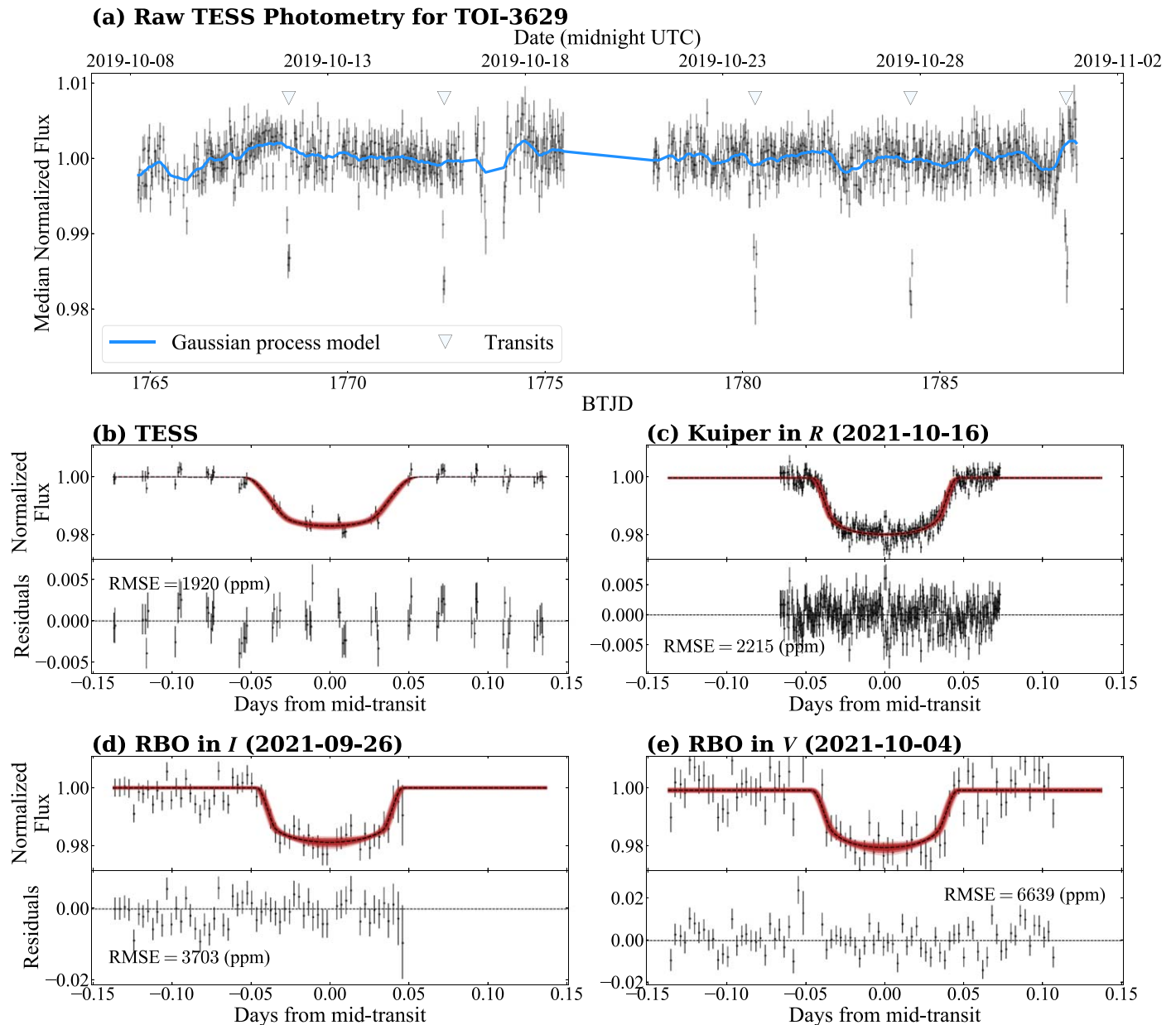


Figure 4. Identical to Figure 3, but for TOI-3629. (a) The median normalized TESS light curve for TOI-3629 derived with `eleanor` along with the best-fitting Gaussian process model. The triangles indicate the mid-transit times. (b)–(e) are the light curves for the TESS, Kuiper, and RBO plotted with model posteriors (shaded regions) from the joint fit to the photometry and RVs.

and variance image calculation. The 1D spectra were extracted following the procedures in Ninan et al. (2018), Kaplan et al. (2019), and Metcalf et al. (2019). The wavelength solution and drift correction were extrapolated using laser frequency comb (LFC) frames obtained from routine calibrations. This extrapolation enables wavelength calibration on the order of $<30 \text{ cm s}^{-1}$ (see Appendix A in Stefánsson et al. 2020), a value which is much smaller than the RV uncertainty for our targets ($>10 \text{ m s}^{-1}$).

The RVs were calculated using a modified version of the `SpEctrum Radial Velocity AnaLyser` code (SERVAL; Zechmeister et al. 2018) optimized for HPF RV extractions (see Metcalf et al. 2019 and Stefánsson et al. 2020 for details). SERVAL employs the template-matching technique to derive RVs (e.g., Anglada-Escudé & Butler 2012) and creates a master

template from the observations to determine the Doppler shift by minimizing the χ^2 statistic. The master template is generated from all observed spectra after masking sky-emission lines and telluric regions identified using a synthetic telluric-line mask generated from `telfit` (Gullikson et al. 2014). The barycentric correction is calculated using `barycorrpy`, a Pythonic implementation (Kanodia & Wright 2018) of the algorithms from Wright & Eastman (2014).

2.8. NEID Spectrograph

NEID is an environmentally stabilized (Stefánsson et al. 2016; Robertson et al. 2019), high-resolution ($R \sim 110,000$) spectrograph installed on the WIYN 3.5 m telescope at KPNO in Arizona (Schwab et al. 2016). NEID features

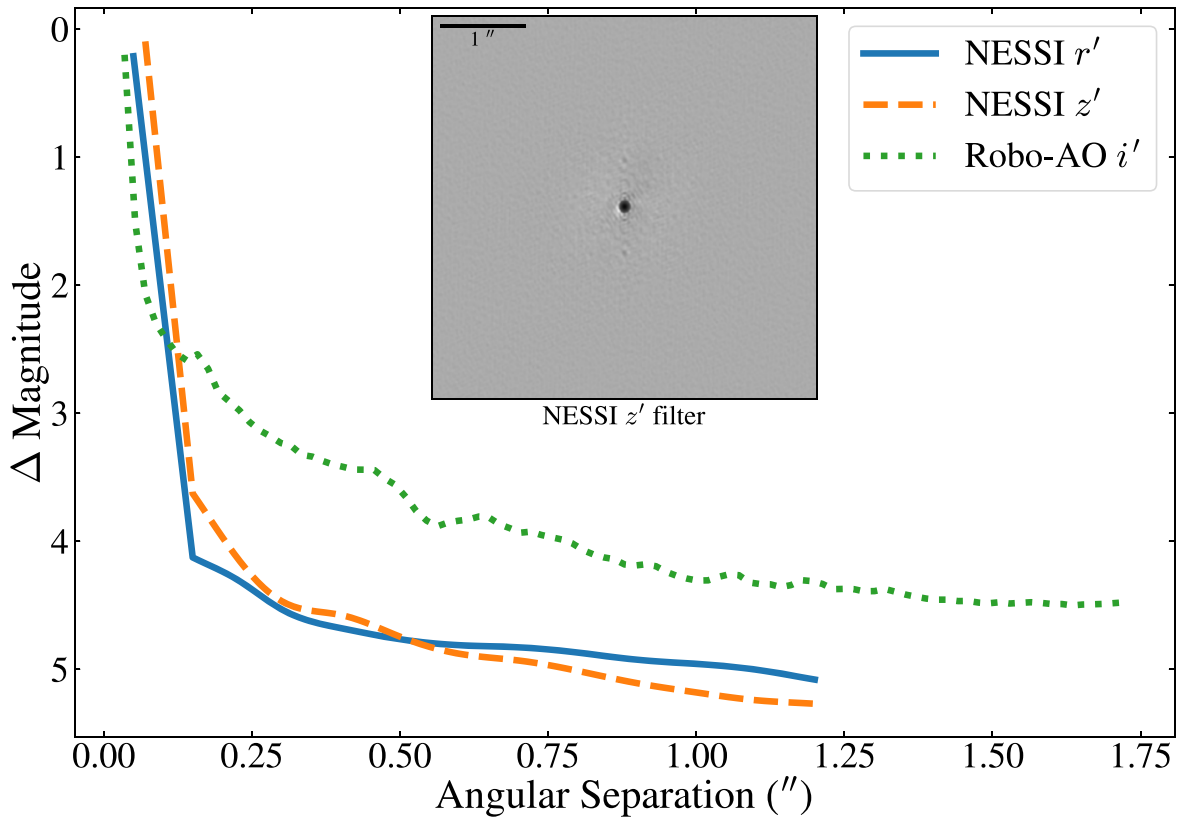


Figure 5. The 5σ contrast curves for TOI-3629 obtained from AO imaging using Robo-AO in the Sloan i' filter and speckle imaging with NESSI in the Sloan r' and z' filters. The data reveal no bright companions at separations of $0''.2 - 1''.75$ from TOI-3629. The inset is the $4''.7 \times 4''.7$ NESSI speckle image centered on TOI-3629 in the Sloan z' filter.

extended red wavelength coverage ($\lambda \sim 3800\text{--}9300 \text{ \AA}$) and a fiber-feed system similar to HPF (Kanodia et al. 2018). Between 2021 September 21 and 2022 January 8, we obtained eight visits of TOI-3714 and five visits of TOI-3629. Observations were obtained in queue mode, and NEID operated in high-resolution mode. The median S/Ns per 1D extracted pixel were 15 and 19, respectively, at 850 nm.

The NEID data were reduced using the NEID Data Reduction Pipeline³⁴ (DRP), and the Level-2 1D extracted spectra were retrieved from the NEID Archive.³⁵ Similar to HPF, to maximize the RV precision from the M dwarf spectra, we measured the RVs using a modified version of the *SERVAL* code (see Stefánsson et al. 2022). We extracted RVs with *SERVAL* using different segments of an order (inner 3000, 5000, or 7000 pixels) and different wavelength ranges (4950–8960 \AA or 5440–8960 \AA). The various combinations of pixel and wavelength ranges produced RVs that, when jointly modeled with photometry and HPF RVs, resulted in identical system parameters (within their 1σ uncertainty). The NEID RVs presented in this work were calculated using the wavelength range from 5440–8920 \AA (order indices 61–104) and the inner most 3000 pixels of each order. This effectively uses the central blaze region of each order and limits the use of the lower-S/N regions near the edge of each order. Table 1 reports the HPF and NEID RVs, the 1σ uncertainties, the S/N per pixel, and the exposure times for TOI-3714 and TOI-3629.

Figures 7 and 8 display the RVs for TOI-3714 and TOI-3629, respectively.

3. Stellar Parameters

3.1. Spectroscopic Parameters

The stellar effective temperature (T_e), surface gravity ($\log g_*$), and metallicity ($[\text{Fe}/\text{H}]$) were calculated using the *HPF-SpecMatch*³⁶ package (Stefánsson et al. 2020), which derives stellar parameters using the empirical template-matching methodology discussed in Yee et al. (2017). It identifies the best-matching spectra from a library of well-characterized stars using χ^2 minimization, creates a composite spectrum using a weighted, linear combination of the five best-matching library spectra, and derives the stellar properties using these weights. When searching for the best-matching library spectra, *HPF-SpecMatch* broadens the stellar templates using a linear limb-darkening law. The reported uncertainty is the standard deviation of the residuals from a leave-one-out cross-validation procedure applied to the entire spectral library in the chosen spectral order.

The HPF spectral library contains 166 stars and spans the following parameter space: $2700 \text{ K} < T_e < 6000 \text{ K}$, $4.3 < \log g_* < 5.3$, and $-0.5 < [\text{Fe}/\text{H}] < 0.5$. The library includes 87 M dwarfs ($T_e \leq 4000 \text{ K}$) of which 37 are early M dwarfs spanning $3500 \text{ K} \leq T_e \leq 4000 \text{ K}$, $4.6 < \log g_* < 4.9$, and $-0.5 < [\text{Fe}/\text{H}] < 0.5$. The spectral matching was performed on

³⁴ <https://neid.ipac.caltech.edu/docs/NEID-DRP/>

³⁵ <https://neid.ipac.caltech.edu/>

³⁶ <https://gummiks.github.io/hpfspecmatch/>

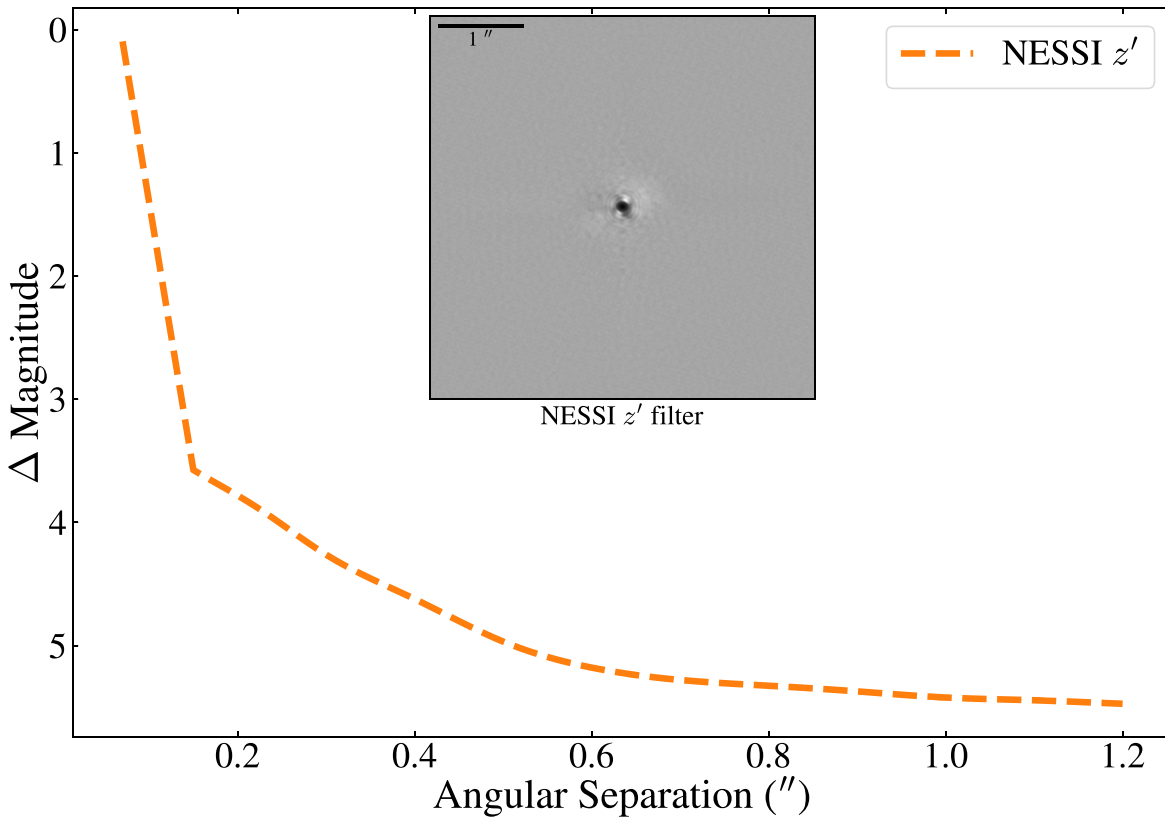


Figure 6. Similar to Figure 5 but for TOI-3714. The 5σ contrast curve for TOI-3714 obtained from speckle imaging using NESSI in the Sloan z' filter. The data reveal no bright companions at separations of $0''.2$ – $1''.75$ from TOI-3714. The inset is the $4''.7 \times 4''.7$ NESSI speckle image centered on TOI-3714 in the Sloan z' filter.

HPF order index 5 (8534–8645 Å) for both targets because this order has little to no telluric contamination. The resolution limit of HPF places a constraint of $v \sin i < 2 \text{ km s}^{-1}$ for both TOI-3714 and TOI-3629. TOI-3714 is determined to have $T_e = 3660 \pm 90 \text{ K}$, $\log g_* = 4.75 \pm 0.05$, and $[\text{Fe}/\text{H}] = 0.1 \pm 0.1$. TOI-3629 is determined to have $T_e = 3870 \pm 90 \text{ K}$, $\log g_* = 4.67 \pm 0.05$, and $[\text{Fe}/\text{H}] = 0.4 \pm 0.1$. Table 2 presents the derived spectroscopic parameters with their uncertainties.

3.2. Spectral Classification

The Large Sky Area Multi-Object Fiber Spectroscopic Telescope (LAMOST) collaboration observed TOI-3714 on 2012 January 11 and TOI-3629 on 2018 November 3 as part of a survey of the Galactic anti-center (Yuan et al. 2015; Xiang et al. 2017). LAMOST is a 4 m telescope equipped with 4000 fibers distributed over a 5° FOV that is capable of acquiring spectra in the optical band (3700–9000 Å) at a resolution $R \approx 1800$ with a limiting magnitude of SDSS $r' = 19 \text{ mag}$ (Cui et al. 2012). The data used in this work are from the public DR7v2.0³⁷ release.

The LAMOST stellar classification pipeline (Zhong et al. 2015) uses stellar templates to identify molecular absorption features (e.g., CaH, TiO) that are typical for M-type stars and reports the subclass of an M dwarf with an accuracy of ± 0.5 subtypes. To be classified as M dwarfs, targets must have (i) a mean S/N > 5 , (ii) a best-matching template that is an M type, and (iii) the spectral indices of the absorption features must be located in the M-type stellar regime identified in Zhong et al.

(2019; $0 < \text{TiO}5 < 1.2$ and $0.6 < \text{CaH}2 + \text{CaH}3 < 2.4$). LAMOST classifies TOI-3714 as an $\text{M}2 \pm 0.5$ dwarf and TOI-3629 as an $\text{M}1 \pm 0.5$ dwarf, which agrees with the derived parameters from HPF-SpecMatch in Section 3.1.

3.3. Spectral Energy Distribution Fitting

To derive model-dependent stellar parameters, we modeled the spectral energy distribution (SED) for each target using the EXOFASTv2 analysis package (Eastman et al. 2019). EXOFASTv2 calculates the bolometric corrections for the SED fit by linearly interpolating the precomputed bolometric³⁸ bolometric in $\log g_*$, T_e , $[\text{Fe}/\text{H}]$, and A_V from the Modules for Experiments in Stellar Astrophysics Isochrones and Stellar Tracks (MIST) model grids (Choi et al. 2016; Dotter 2016).

The SED fits use Gaussian priors on the (i) Two Micron All Sky Survey (2MASS) J , H , K magnitudes, Sloan g' , r' , i' magnitudes and Johnson B , V magnitudes from Henden et al. (2018), and Wide-field Infrared Survey Explorer magnitudes (WISE; Wright et al. 2010); (ii) $\log g_*$, T_e , and $[\text{Fe}/\text{H}]$ derived from HPF-SpecMatch, and (iii) the geometric distance calculated from Bailer-Jones et al. (2021) for each respective star. We apply an upper limit to the visual extinction based on estimates of Galactic dust (Green et al. 2019) calculated at the distance determined by Bailer-Jones et al. (2021). The $R_V = 3.1$ reddening law from Fitzpatrick (1999) is used to convert the extinction from Green et al. (2019) to a visual magnitude extinction. Table 2 contains the stellar priors and derived stellar parameters with their uncertainties. The model-dependent

³⁷ <http://dr7.lamost.org/>

³⁸ http://waps.cfa.harvard.edu/MIST/model_grids.html#

Table 1
RVs of TOI-3714 and TOI-3629

BJD _{TDB}	RV (m s ⁻¹)	σ (m s ⁻¹)	S/N ^a	Exp. Time (s)	Instrument
TOI-3714:					
2459450.941268	-196	23	44	1890	HPF
2459451.948741	163	25	42	1890	HPF
2459452.941751	-183	22	47	1890	HPF
2459458.924675	15	25	41	1890	HPF
2459511.784103	60	23	44	1890	HPF
2459512.783671	29	23	46	1890	HPF
2459516.779359	209	26	40	1890	HPF
2459516.995256	64	20	50	1890	HPF
2459518.748189	119	30	35	1890	HPF
2459518.992056	135	23	44	1890	HPF
2459519.985625	-189	22	46	1890	HPF
2459571.844384	-103	29	34	1890	HPF
2459479.884140	71	12	15	1800	NEID
2459503.998300	27	15	11	1200	NEID
2459520.927772	77	11	15	1800	NEID
2459531.844720	58	10	16	1800	NEID
2459533.801149	89	9	18	1800	NEID
2459560.766674	-244	14	12	1800	NEID
2459586.625543	-239	11	15	1800	NEID
2459587.851477	91	20	9	1800	NEID
TOI-3629:					
2459232.579925	26	16	52	1890	HPF
2459233.576944	-24	18	48	1890	HPF
2459448.764453	28	13	66	1890	HPF
2459451.979492	1	18	49	1890	HPF
2459452.761162	5	15	59	1890	HPF
2459453.979751	-72	16	58	1890	HPF
2459455.739966	5	14	62	1890	HPF
2459457.974338	-42	13	64	1890	HPF
2459460.962548	-16	15	57	1890	HPF
2459461.955253	-91	18	48	1890	HPF
2459470.709176	-47	17	51	1890	HPF
2459471.707553	9	14	60	1890	HPF
2459475.919121	23	20	47	1890	HPF
2459477.918199	-72	18	50	1890	HPF
2459480.910306	-10	24	51	945	HPF
2459485.896427	-57	22	41	1890	HPF
2459499.627624	64	17	54	1890	HPF
2459507.814595	24	23	40	1890	HPF
2459516.581430	-20	15	59	1890	HPF
2459543.736198	11	15	60	1890	HPF
2459588.597139	-57	15	56	1890	HPF
2459592.597117	-48	15	60	1890	HPF
2459593.588844	44	16	54	1890	HPF
2459478.965087	-20	6	22	1800	NEID
2459479.794197	28	6	22	1800	NEID
2459528.888224	-34	14	11	1800	NEID
2459532.843589	-38	8	19	1800	NEID
2459546.840787	62	15	11	1800	NEID

Note.

^a The HPF and NEID S/N are the median values per 1D extracted pixel at 1070 nm and 850 nm, respectively.

mass and radius are (i) $0.53 \pm 0.02 M_{\odot}$ and $0.51 \pm 0.01 R_{\odot}$ for TOI-3714 and (ii) $0.63 \pm 0.02 M_{\odot}$ and $0.60^{+0.02}_{-0.01} R_{\odot}$ for TOI-3629.

The masses and radii are identical within their respective 1σ uncertainties to the parameters from the TIC catalog for TOI-3714 ($0.51 \pm 0.02 M_{\odot}$ and $0.51 \pm 0.02 R_{\odot}$) and TOI-3629 ($0.60 \pm 0.02 M_{\odot}$ and $0.61 \pm 0.02 R_{\odot}$).

3.4. Stellar Rotation Period

If we assume TOI-3714 and TOI-3629 are well aligned with the orbit of their transiting planets ($\sin i_{*} \sim 1$), the constraint of $v \sin i_{*} < 2 \text{ km s}^{-1}$ from HPF spectra requires each star to have a rotation period of >10 days. We do not search for photometric modulation in the `corr_flux` because long-period (>10 day) astrophysical signals, such as starspot-induced photometric variability, are attenuated when removing systematics with `eleanor` (Feinstein et al. 2019), similar to how long-period rotation signals are damped and distorted in Kepler PDCSAP light curves (Gilliland et al. 2015; Van Cleve et al. 2016). We instead searched for photometric modulation in TESS data using the `TESS-SIP` package (Hedges et al. 2020), which is designed to simultaneously create a Lomb–Scargle periodogram and detrend systematics. `TESS-SIP` uses a linear model with two components: (i) regressors (by default two principal components and a mean offset) to remove instrument systematics and (ii) a sinusoidal component to fit a power spectrum. Only one sector of TESS data exist for each target, and we limit this search to a rotation period range of 1–30 days. For this search, the transits were excised using the duration and ephemeris from the QLP. `TESS-SIP` recovers no significant period for either TOI-3714 and TOI-3629 between 1 and 30 days.

We also used data from ZTF DR11 in the `zg` and `zr` filters to search for any long-period signals caused by activity-induced photometric modulations in the target stars. This search used the generalized Lomb–Scargle (GLS) periodogram (Zechmeister & Kürster 2009) because it has been shown to successfully recover rotation periods in photometry (see VanderPlas 2018; Canto Martins et al. 2020; Reinhold & Hekker 2020). The GLS periodogram is based on Fourier decomposition and provides peaks in the frequency space where the highest peak in the periodogram is associated with the period of the best-fit sine wave that minimizes the χ^2 statistic. We use the `GLS39` package to perform this analysis and only consider significant peaks where the false-alarm probability (FAP), as calculated following Zechmeister & Kürster (2009), is below a threshold of 0.1%. Data within transits were excised using the duration and ephemeris from the QLP. A significant peak (FAP $< 0.1\%$) of ~ 23.6 days was found in both the `zr` and `zg` photometry of TOI-3714. A significant peak (FAP $< 0.1\%$) of ~ 29.5 days was found in the `zr` photometry while no significant peaks were seen in the `zg` photometry for TOI-3629.

To derive the rotation period and an estimate of its uncertainty, we modeled the ZTF photometry using the `juliet` analysis package (Espinoza et al. 2019), which performs the parameter estimation using the dynamic nested-sampling algorithm `dynesty` (Speagle 2020). The photometric model is a Gaussian process noise model using the approximate quasiperiodic covariance function presented in Foreman-Mackey et al. (2017) of the form:

$$k(\tau) = \frac{B}{2 + C} e^{-\tau/L} \left[\cos\left(\frac{2\pi\tau}{P_{\text{GP}}}\right) + (1 + C) \right], \quad (1)$$

where τ is the time of observation while B , C , L , and P_{GP} are the hyperparameters of the covariance function. B and C represent the weight of the exponential term with a decay constant of L (in days). P_{GP} determines the periodicity of the

³⁹ <https://github.com/mzechmeister/GLS>

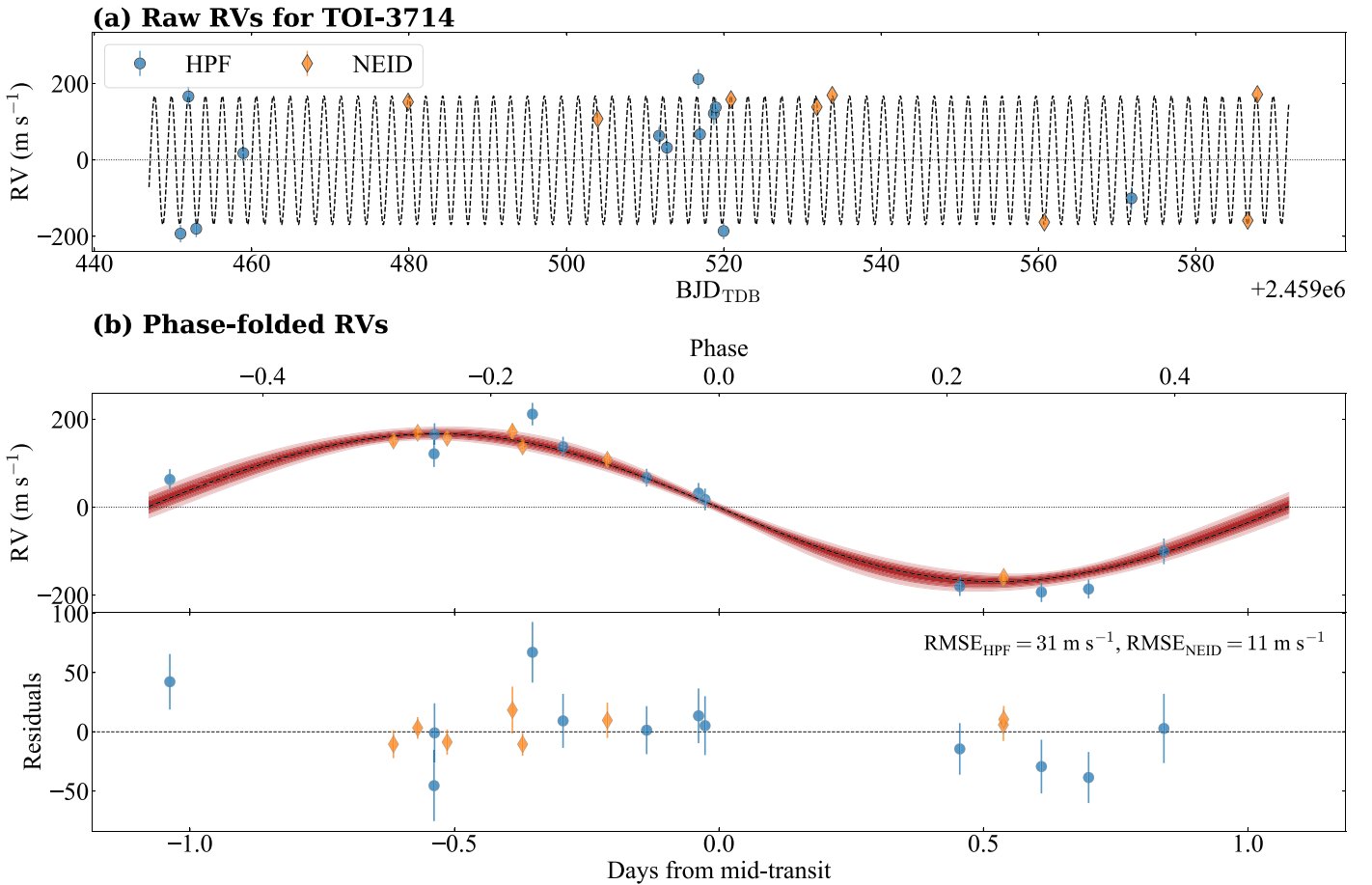


Figure 7. (a) RVs for TOI-3714, after subtracting the instrumental offsets, derived with modified versions of `SERVAL`. (b) Phase-folded RVs plotted with model posteriors. For each panel, the dashed line is the best-fitting Keplerian model. The shaded regions denote the 1σ (darkest), 2σ , and 3σ (lightest) extent of the model posteriors. The modeling is described in Section 4.

quasiperiodic oscillations, which is interpreted as the stellar rotation period. This kernel is able to reproduce the behavior of a more traditional quasiperiodic covariance function and has allowed for computationally efficient inference of stellar rotation periods even for large data sets that are not uniformly sampled (e.g., Angus et al. 2018). The photometric model includes a simple white-noise model σ_{phot} in the form of a jitter term that is added in quadrature to the error bars of each filter.

The fit for each star uses a uniform prior on the Gaussian process period of 1–1500 days where the upper limit coincides with the baseline of existing ZTF data. For TOI-3714, the zr and zg data are jointly modeled and share the value of P_{GP} , while the nuisance parameters (B , C , L , and σ_{phot}) are different for each filter. For TOI-3629, we only model the zr photometry. Figure 9 displays the ZTF photometry folded to the median value of P_{GP} and the posterior distribution for P_{GP} , which we interpret as the rotation period. The measured rotation period is 23.3 ± 0.3 days, which suggests that TOI-3714 most likely has an age between 0.7 and 5.1 Gyr after adopting the classification scheme of Newton et al. (2016). This age range is consistent with the rotation period and age relationship from Engle & Guinan (2018) and the values from our model-dependent SED fit. We are unable to place any additional constraint on the rotation period of TOI-3629 as the fit does not recover a significant period ($P_{\text{GP}} = 750^{+450}_{-460}$ days).

3.5. Galactic Kinematics

The UVW velocities in the barycentric frame were derived with `galpy` (Bovy 2015) using the Gaia EDR3 proper motions and the systemic velocity derived from HPF. The values in Table 2 are in a right-handed coordinate system (Johnson & Soderblom 1987), where UVW are positive in the directions of the Galactic center, Galactic rotation, and the north Galactic pole, respectively. The UVW velocities in Table 2 are also provided with respect to the local standard of rest using the solar velocities and uncertainties from Schönrich et al. (2010). The BANYAN Σ algorithm (Gagné et al. 2018), which uses sky positions, proper motions, parallaxes, and RVs to constrain cluster membership probabilities, classifies both TOI-3714 and TOI-3629 as field stars showing no associations with known young clusters.

Using kinematic selection criteria from Bensby et al. (2003), TOI-3714 is classified as a member of the thin disk ($P_{\text{Thick}}/P_{\text{Thin}} = 0.02$). The classification for TOI-3629 is ambiguous as the relative probability of thick disk to thin disk is $P_{\text{Thick}}/P_{\text{Thin}} = 1.1$. We note that TOI-3629 has a large Galactic tangential velocity ($|V_T| = 100.7 \pm 0.5 \text{ km s}^{-1}$) with respect to the local standard of rest. Hwang & Zakamska (2020) used Galactic models to calculate the age distribution for different tangential velocity bins and determined a star with a tangential velocity in the range $100\text{--}120 \text{ km s}^{-1}$ has a $\sim 55\%$ chance of belonging to the thick disk and an estimated age of

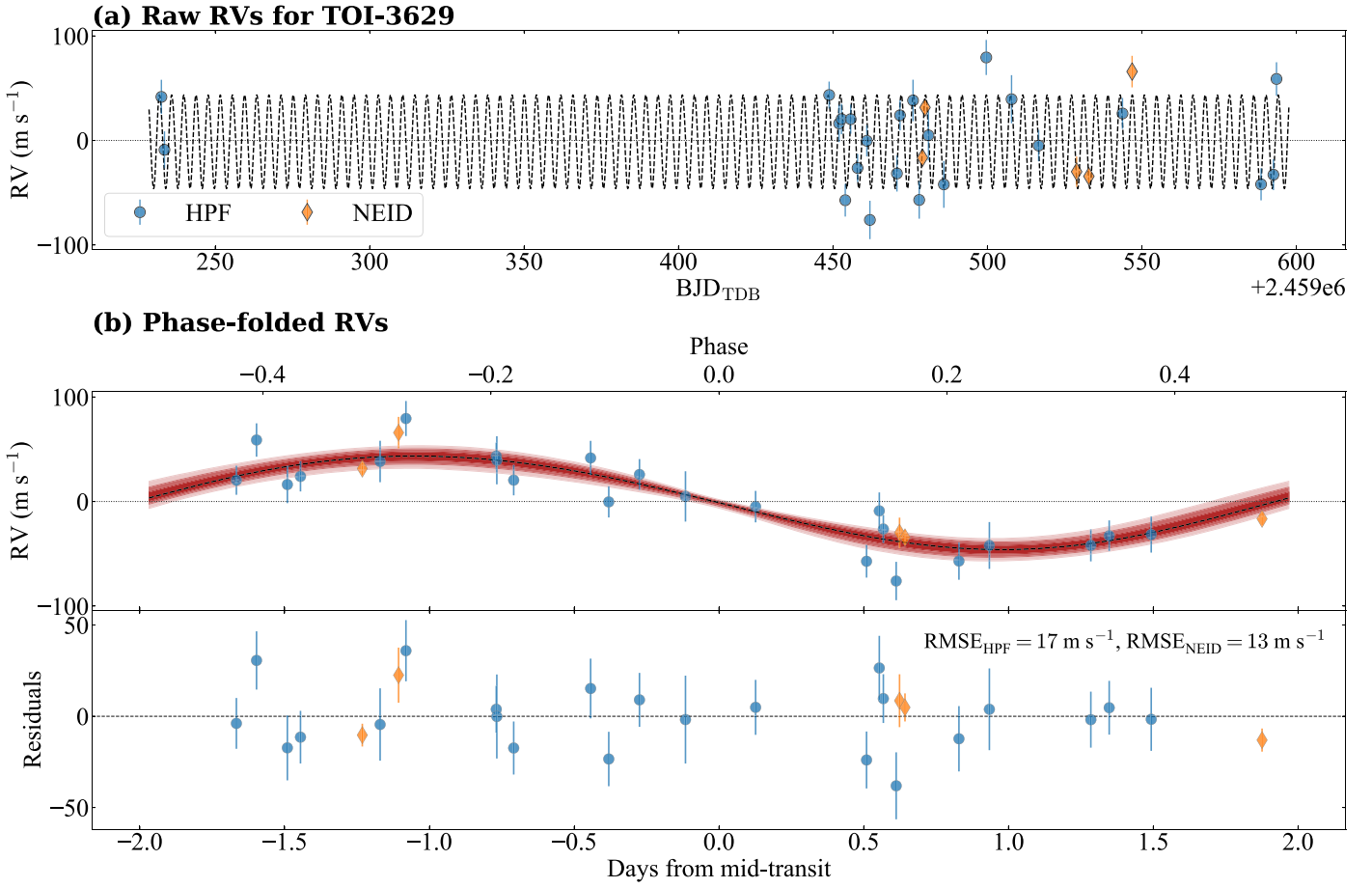


Figure 8. Identical to Figure 7, but for TOI-3629. (a) RVs for TOI-3629, after subtracting the instrumental offsets. (b) Phase-folded RVs plotted with model posteriors.

7 ± 2 Gyr. While we cannot unambiguously classify TOI-3629 as a thick-disk star, its high tangential velocity suggests that its age is most likely >5 Gyr.

4. Photometric and RV Modeling

We use the `juliet` analysis package to jointly model the TESS photometry, ground-based photometry, and velocimetry and perform the parameter estimation using `dynesty`. `juliet` models the RVs with a standard Keplerian RV curve generated from the `radvel` (Fulton et al. 2018) package and models the light curves with a transit model generated from the `batman` package (Kreidberg 2015). The limb-darkening parameters are sampled from uniform priors following the parameterization presented in Kipping (2013a). For the long-cadence TESS photometry, the transit model utilizes the supersampling option in `batman` with exposure times of 30 min and a supersampling factor of 30. The photometric model also includes a dilution factor, D , for TESS representing the ratio between the out-of-transit flux of the host star to that of all stars within the photometric aperture. We include this term for TESS data because `eleanor` does not correct for dilution from nearby stars despite the large apertures adopted (see Figures 1 and 2). Both the photometric and RV models include a simple white-noise model parameterized as a jitter term that is added in quadrature to the error bars of each data set. To account for correlated noise in the TESS light curves, each fit includes a Gaussian process noise model of the same form described in Section 3.4.

Tables 3 and 4 provide a summary of the priors used for the fit along with the inferred system parameters and the confidence intervals (16th – 84th percentiles) for TOI-3714 and TOI-3629, respectively. Figures 3, 4, 7, and 8 display the model posteriors for each system. The modeling reveals that (i) TOI-3714 b is a hot Jupiter ($M_2 = 0.70 \pm 0.03 M_J$ and $R_2 = 1.01 \pm 0.03 R_J$) orbiting its host star on a nearly circular orbit with a period of 2.154849 ± 0.000001 days and (ii) TOI-3629 b is a hot Jupiter ($M_2 = 0.26 \pm 0.02 M_J$ and $R_2 = 0.74 \pm 0.02 R_J$) orbiting its host star on a nearly circular orbit with a period of $3.936551^{+0.000005}_{-0.000006}$ days.

To determine if the low eccentricity of the orbits is consistent with tidal evolution, we estimate the timescales for circularization using the formalism of Jackson et al. (2008). For the tidal quality factors, we assume each hot Jupiter is comparable to Jupiter and adopt a value of $Q_p = 10^5$ (see Goldreich & Soter 1966; Lainey et al. 2009; Lainey 2016). We adopt a nominal value of $Q_* = 10^7$ for early M dwarfs based on the modeling of Gallet et al. (2017). Using the orbit parameters from joint modeling of each system and the stellar parameters, the timescale for circularization is <0.1 Gyr for both systems, suggesting that these systems should be consistent with a circular orbit. If we adopt a larger value of $Q_p = 10^7 - 10^9$ (based on upper limits from Bonomo et al. 2017) the circularization timescale can exceed 10 Gyr, and these systems may be able to retain a nonzero eccentricity. The RVs are able to place upper 3σ limits on eccentricity are $e < 0.12$ for TOI-3714 b and $e < 0.20$ for TOI-3629 b, revealing that even if these systems were not fully circularized, the planets are on low-eccentricity orbits.

Table 2
Summary of Stellar Parameters

Parameter	Description	TOI-3714	TOI-3629	Reference
Main Identifiers:				
TIC	...	155867025	455784423	TIC
Gaia EDR3	...	178924390478792320	2881820324294985856	Gaia EDR3
Coordinates, Proper Motion, Distance, Maximum Extinction, and Spectral Type:				
α_{J2016}	R.A. (RA)	04:38:12.56	23:59:10.42	Gaia EDR3
δ_{J2016}	decl. (Dec)	39:27:28.77	39:18:51.32	Gaia EDR3
μ_α	Proper motion (R.A., mas yr ⁻¹)	19.83 ± 0.03	185.71 ± 0.01	Gaia EDR3
μ_δ	Proper motion (decl., mas yr ⁻¹)	-70.74 ± 0.02	1.01 ± 0.01	Gaia EDR3
l	Galactic longitude	163.30437	112.02292	Gaia EDR3
b	Galactic latitude	-5.02268	-22.44783	Gaia EDR3
d	Geometric distance (pc)	112.5 ^{+0.2} _{-0.4}	129.7 ± 0.3	Bailer-Jones
$A_{V,max}$	Maximum visual extinction	0.02	0.01	Green
Spectral Type	...	M2 ± 0.5	M1 ± 0.5	LAMOST
Broadband Photometric Magnitudes:				
B	Johnson B mag	16.8 ± 0.2	16.1 ± 0.1	APASS
V	Johnson V mag	15.24 ± 0.09	14.63 ± 0.05	APASS
g'	Sloan g' mag	15.9 ± 0.1	15.33 ± 0.04	APASS
r'	Sloan r' mag	14.73 ± 0.09	14.06 ± 0.05	APASS
i'	Sloan i' mag	13.66 ± 0.09	13.12 ± 0.07	APASS
J	J mag	11.74 ± 0.02	11.42 ± 0.03	2MASS
H	H mag	11.06 ± 0.02	10.73 ± 0.03	2MASS
K_s	K_s mag	10.85 ± 0.02	10.55 ± 0.02	2MASS
W1	WISE1 mag	10.72 ± 0.02	10.48 ± 0.02	WISE
W2	WISE2 mag	10.68 ± 0.02	10.52 ± 0.02	WISE
W3	WISE3 mag	10.5 ± 0.1	10.38 ± 0.07	WISE
Spectroscopic Parameters^a:				
T_e	Effective temperature (K)	3660 ± 90	3870 ± 90	This work
$\log g_*$	Surface gravity (cgs)	4.75 ± 0.05	4.67 ± 0.05	This work
[Fe/H]	Metallicity (dex)	0.1 ± 0.1	0.4 ± 0.1	This work
$v \sin i_*$	Rotational broadening (km s ⁻¹)	<2	<2	This work
Model-dependent Stellar SED and Isochrone Fit Parameters^b:				
M_*	Mass (M_\odot)	0.53 ± 0.02	0.63 ± 0.02	This work
R_*	Radius (R_\odot)	0.51 ± 0.01	0.60 ^{+0.02} _{-0.01}	This work
ρ_*	Density (g cm ⁻³)	5.8 ^{+0.4} _{-0.3}	4.0 ± 0.2	This work
A_v	Visual extinction (mag)	0.011 ± 0.007	0.005 ± 0.003	This work
Age ^c	Age (Gyr)	0.7–5.1	7 ± 2	This work
Other Stellar Parameters:				
RV	Systemic RV (km s ⁻¹)	36.4 ± 0.2	-24.83 ± 0.06	This work
P_{rot}	Stellar rotation period (days)	23.3 ± 0.3	...	This work
U, V, W	Barycentric Galactic velocities (km s ⁻¹)	-43.5 ± 0.2, -23.9 ± 0.1, -20.43 ± 0.05	-91.9 ± 0.2, -72.0 ± 0.1, -13.06 ± 0.06	This work
$(U, V, W)_{LSR}$	Galactic velocities w.r.t. LSR ^d (km s ⁻¹)	-32.4 ± 0.8, -11.7 ± 0.5, -13.2 ± 0.4	-80.8 ± 0.8, -59.7 ± 0.5, -5.8 ± 0.4	This work

Notes.

^a Derived with the HPF-SpecMatch package.

^b Derived with the EXOFASTv2 package using MIST isochrones.

^c We report the age estimate of TOI-3714 using the rotation period and classification from Newton et al. (2016). The age for TOI-3629 is from Galactic models based on its tangential velocity.

^d Calculated using the solar velocities from Schönrich et al. (2010).

References. TIC (Stassun et al. 2019), Gaia EDR3 (Gaia Collaboration et al. 2021), Bailer-Jones (Bailer-Jones et al. 2021), Green (Green et al. 2019), LAMOST (Zhong et al. 2019), American Association of Variable Star Observers Photometric All-Sky Survey (APASS; Henden et al. 2018), 2MASS (Cutri et al. 2003), WISE (Wright et al. 2010).

5. Discussion

5.1. Constraints on Unresolved Stellar Companions

For both targets, the stellar density derived from the transit fit (see Seager & Mallén-Ornelas 2003; Winn 2010) in Section 4

is consistent with the value derived with an SED fit (Section 3). Following the methodology presented in Kanodia et al. (2020), we place limits on any spatially unresolved stellar companions to our targets by quantifying the lack of flux from a secondary stellar object in the HPF spectra. The highest S/N spectrum for

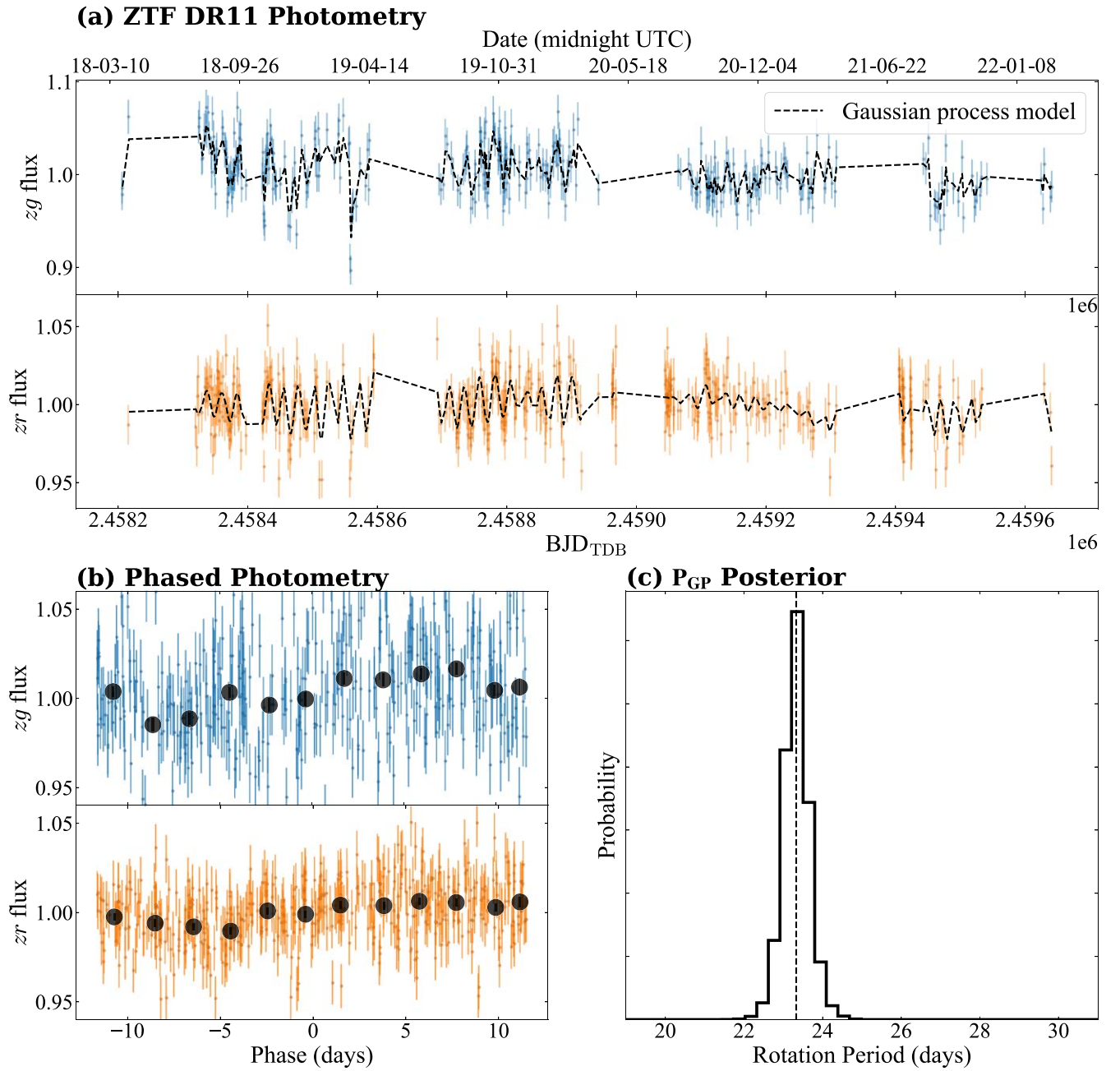


Figure 9. (a) ZTF photometry for TOI-3714 in each filter along with the best-fitting Gaussian process model for reference. (b) Ground-based ZTF photometry from panel (a) phased to the derived rotation period. The large black points represent 2 days bins of the phased photometry. (c) Posterior distribution of the rotation period from the Gaussian process model. The derived rotation period is 23.3 ± 0.3 days.

each target is parameterized as a linear combination of a primary M dwarf⁴⁰ and a secondary stellar companion. The flux ratio between the secondary and primary star, F , is calculated as:

$$S_{\text{obs}} = A((1 - x)S_{\text{primary}} + (x)S_{\text{secondary}}), \quad (2)$$

$$F = \frac{x}{1 - x}, \quad (3)$$

where S_{obs} is the observed spectrum, S_{primary} is the primary spectrum, $S_{\text{secondary}}$ represents the secondary spectrum, and A is

⁴⁰ GJ_205 and BD+29_2279 for TOI-3714 and TOI-3629, respectively, as identified by HPF-SpecMatch.

the normalization constant. For a given primary and secondary template, we (i) shift the secondary spectrum in velocity space, (ii) add this shifted spectrum to the primary spectrum, and (iii) fit for the value of x that best fits the observed spectrum. We limit the secondary spectral type to M dwarfs earlier than M7 and to the orders where telluric absorption is minimal.

Figure 10 presents the results from HPF order index 17 spanning 10450 – 10580 Å. We place a conservative upper limit for a secondary of flux ratio = 0.07 or $\Delta\text{mag} \simeq 2.9$ for both TOI-3714 and TOI-3629. As shown in Figure 10, there is no significant flux contamination at $|\Delta v| > 5 \text{ km s}^{-1}$. We perform this secondary light analysis for velocity offsets from 5–100 km s^{-1} , where the lower limit coincides with the

Table 3
System Parameters for TOI-3714

Parameter	Units	Prior	Value			
Photometric Parameters						
Linear Limb-darkening Coefficient ^a	q_1	$\mathcal{U}(0, 1)$	TESS $0.4^{+0.2}_{-0.1}$	RBO (08-16) 0.5 ± 0.2	RBO (11-19) 0.5 ± 0.2	ARCTIC 0.4 ± 0.1
Quadratic Limb-darkening Coefficient ^a	q_2	$\mathcal{U}(0, 1)$	0.4 ± 0.2	$0.2^{+0.2}_{-0.1}$	$0.2^{+0.2}_{-0.1}$	0.5 ± 0.1
Photometric Jitter	σ_{phot} (ppm)	$\mathcal{J}(10^{-6}, 10^3)$	$0.007^{+1.765}_{-0.007}$	$0.003^{+1.431}_{-0.003}$	$0.03^{+11.3}_{-0.03}$	20^{+778}_{-20}
Dilution Factor	D	$\mathcal{U}(0, 2)$	0.87 ± 0.02
RV Parameters						
Systemic velocity	γ (m s ⁻¹)	$\mathcal{U}(-10^3, 10^3)$	HPF -3 ± 7		NEID -81 ± 6	
RV Jitter	σ_{RV} (m s ⁻¹)	$\mathcal{J}(10^{-3}, 10^3)$	4^{+20}_{-4}		7^{+6}_{-3}	
Orbital Parameters:						
Orbital Period	P (days)	$\mathcal{N}(2.15, 0.01)$		2.154849 ± 0.000001		
Time of Transit Center	T_C (BJD _{TDB})	$\mathcal{N}(2458840.51, 0.01)$		2458840.5093 ± 0.0004		
$\sqrt{e} \cos \omega$		$\mathcal{U}(-1, 1)$		0.0 ± 0.1		
$\sqrt{e} \sin \omega$		$\mathcal{U}(-1, 1)$		0.1 ± 0.1		
Semi-amplitude velocity	K (m s ⁻¹)	$\mathcal{J}(1, 10^3)$		169^{+6}_{-5}		
Scaled Radius	R_p/R_*	$\mathcal{U}(0, 1)$		0.204 ± 0.003		
Impact Parameter	b	$\mathcal{U}(0, 1)$		$0.26^{+0.08}_{-0.1}$		
Scaled Semimajor Axis	a/R_*	$\mathcal{J}(1, 100)$		$11.5^{+0.4}_{-0.5}$		
Gaussian Process Hyperparameters:						
B	Amplitude (ppm)	$\mathcal{J}(10^{-4}, 10^{12})$		$1.8^{+2.3}_{-0.7}$		
C	Additive Factor	$\mathcal{J}(10^{-3}, 10^3)$		1^{+50}_{-1}		
L	Length scale (days)	$\mathcal{J}(10^{-3}, 10^3)$		3^{+6}_{-2}		
P_{GP}	Period (days)	$\mathcal{J}(1.0, 100)$		11^{+30}_{-8}		
Derived Parameters:						
Eccentricity	e	...		$0.03^{+0.03}_{-0.02}, 3\sigma < 0.12$		
Argument of Periastron	ω (degrees)	...		100^{+61}_{-200}		
Orbital Inclination	i (degrees)	...		88.7 ± 0.5		
Transit Duration	T_{14} (hours)	...		$1.66^{+0.02}_{-0.01}$		
Mass	M_p (M_J)	...		0.70 ± 0.03		
Radius	R_p (R_J)	...		1.01 ± 0.03		
Surface Gravity	$\log g_p$ (cgs)	...		3.25 ± 0.04		
Density	ρ_p (g cm ⁻³)	...		0.85 ± 0.08		
Semimajor Axis	a (au)	...		0.027 ± 0.001		
Average Incident Flux	$\langle F \rangle$ (10 ⁸ erg s ⁻¹ cm ⁻²)	...		$0.74^{+0.06}_{-0.07}$		
Equilibrium Temperature ^b	T_{eq} (K)	...		750 ± 20		

Notes.

^a Using the q_1 and q_2 parameterization from Kipping (2013a).

^b The planet is assumed to be a blackbody, and we ignore heat redistribution.

spectral resolution of HPF ($\sim 5.5 \text{ km s}^{-1}$). The degeneracy between the primary and secondary spectra at velocity offsets $< 5 \text{ km s}^{-1}$ prevent any meaningful flux ratio constraints at those velocity offsets.

5.2. Constraints on Unresolved Bound Companions

We use `thejoker` (Price-Whelan et al. 2017) to perform a rejection sampling analysis on the residuals for the HPF RVs to constrain the existence of additional signals within the HPF RVs. This analysis used a log-uniform prior for the period (between 1 day and twice the HPF RV baseline), the Beta distribution from Kipping (2013b) as a prior for the eccentricity, and a uniform prior for the argument of pericenter and the orbital phase. For both TOI-3714 and TOI-3629, we analyzed $> 10^8$ (2^{28}) samples with `thejoker` and had a total acceptance rate of $< 3\%$. The surviving samples place an upper limit on any low-inclination ($\sin i \sim 1$) companions of $M < 3.1 M_J$ ($K < 300 \text{ m s}^{-1}$) within 0.6 au ($P < 242$ days) for

TOI-3714 and $M < 2.9 M_J$ ($K < 160 \text{ m s}^{-1}$) within 1.4 au ($P < 722$ days) for TOI-3629.

Gaia EDR3 provides an additional constraint on the presence of close-in, massive companions with the renormalized unit weight error (RUWE) statistic. Lindegren et al. (2021) note that the RUWE, or the square root of the reduced χ^2 statistic that has been corrected for calibration errors, is sensitive to the photocentric motions of unresolved objects. In systems with massive companions on orbital periods much shorter than the baseline of Gaia (34 months for EDR3), the astrometric motion of the primary star around the center of mass may appear as noise when adopting a single-star astrometric solution (e.g., Kervella et al. 2019; Kiefer et al. 2019). $\text{RUWE} \gtrsim 1.4$ is a threshold that correlates with the existence of an unresolved stellar companion in recent studies of stellar binaries (e.g., Belokurov et al. 2020; Gandhi et al. 2020; Penoyre et al. 2020; Stassun & Torres 2021). With RUWE values of 1.15 and 1.05, Gaia EDR3 suggests TOI-3714 and TOI-3629 do not have

Table 4
System Parameters for TOI-3629

Parameter	Units	Prior	Value			
Photometric Parameters			TESS	RBO (09-26)	RBO (10-04)	Kuiper
Linear Limb-darkening Coefficient ^a	q_1	$\mathcal{U}(0, 1)$	0.4 ± 0.2	$0.3^{+0.2}_{-0.1}$	$0.6^{+0.2}_{-0.3}$	0.7 ± 0.2
Quadratic Limb-darkening Coefficient ^a	q_2	$\mathcal{U}(0, 1)$	$0.3^{+0.3}_{-0.2}$	0.5 ± 0.3	0.3 ± 0.2	0.21 ± 0.09
Photometric Jitter	σ_{phot} (ppm)	$\mathcal{J}(10^{-6}, 10^3)$	$0.03^{+423.61}_{-0.03}$	$0.001^{+0.442}_{-0.001}$	$0.03^{+16.45}_{-0.03}$	10^{+421}_{-10}
Dilution Factor	D	$\mathcal{U}(0, 2)$	0.90 ± 0.04
RV Parameters			HPF		NEID	
Systemic velocity	γ (m s ⁻¹)	$\mathcal{U}(-10^3, 10^3)$	-15 ± 3		-4^{+10}_{-8}	
RV Jitter	σ_{RV} (m s ⁻¹)	$\mathcal{J}(10^{-3}, 10^3)$	5^{+5}_{-3}		16^{+10}_{-7}	
Orbital Parameters:						
Orbital Period	P (days)	$\mathcal{N}(3.94, 0.01)$	$3.936551^{+0.000005}_{-0.000006}$			
Time of Transit Center	T_C (BJD _{TDB})	$\mathcal{N}(2458784.26, 0.01)$	2458784.256 ± 0.001			
$\sqrt{e} \cos \omega$		$\mathcal{U}(-1, 1)$	-0.1 ± 0.1			
$\sqrt{e} \sin \omega$		$\mathcal{U}(-1, 1)$	$-0.1^{+0.2}_{-0.1}$			
Semi-amplitude velocity	K (m s ⁻¹)	$\mathcal{J}(1, 10^3)$	45 ± 4			
Scaled Radius	R_p/R_*	$\mathcal{U}(0, 1)$	0.126 ± 0.002			
Impact Parameter	b	$\mathcal{U}(0, 1)$	0.2 ± 0.1			
Scaled Semimajor Axis	a/R_*	$\mathcal{J}(1, 100)$	15.4 ± 0.8			
Gaussian Process Hyperparameters:						
B	Amplitude (ppm)	$\mathcal{J}(10^{-4}, 10^{12})$	$1.8^{+1.5}_{-0.5}$			
C	Additive Factor	$\mathcal{J}(10^{-3}, 10^3)$	3^{+80}_{-3}			
L	Length scale (days)	$\mathcal{J}(10^{-3}, 10^3)$	$0.8^{+1.6}_{-0.4}$			
P_{GP}	Period (days)	$\mathcal{J}(1.0, 100)$	9^{+37}_{-8}			
Derived Parameters:						
Eccentricity	e	...	$0.05^{+0.05}_{-0.04}, 3\sigma < 0.20$			
Argument of Periastron	ω (degrees)	...	-110^{+200}_{-40}			
Orbital Inclination	i (degrees)	...	89.1 ± 0.5			
Transit Duration	T_{14} (hours)	...	2.20 ± 0.03			
Mass	M_p (M_J)	...	0.26 ± 0.02			
Radius	R_p (R_J)	...	0.74 ± 0.02			
Surface Gravity	$\log g_p$ (cgs)	...	$3.09^{+0.06}_{-0.07}$			
Density	ρ_p (g cm ⁻³)	...	0.8 ± 0.1			
Semimajor Axis	a (au)	...	0.043 ± 0.002			
Average Incident Flux	$\langle F \rangle$ (10^8 erg s ⁻¹ cm ⁻²)	...	0.53 ± 0.06			
Equilibrium Temperature ^b	T_{eq} (K)	...	690 ± 20			

Notes.

^a Using the q_1 and q_2 parameterization from Kipping (2013a).

^b The planet is assumed to be a blackbody, and we ignore heat redistribution.

massive stellar companions on short periods ($\gtrsim 0.1$ –3 years). Instead, these systems are in agreement with a single-star astrometric solution.

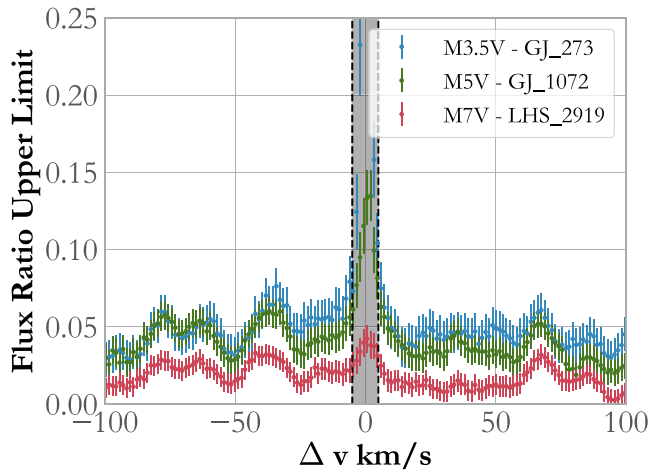
5.3. Constraints on Resolved Bound Companions

We also use results from Gaia EDR3 to determine if either star has a wide separation stellar companion. El-Badry et al. (2021) provide a list of spatially resolved binary stars from an analysis of proper motions. TOI-3629 is not contained in the catalog but TOI-3714 is identified as having a white dwarf stellar companion, Gaia EDR3 178924390476838784 (TIC 662037581). Systems in El-Badry et al. (2021) are flagged as having a white dwarf companion based on the location of the companion on the Gaia color–absolute magnitude diagram (El-Badry & Rix 2018). This object has a negligible probability ($\sim 0.0006\%$) of being the chance alignment of a background source with spurious parallax and proper motion measurements. The white dwarf companion is located at a projected

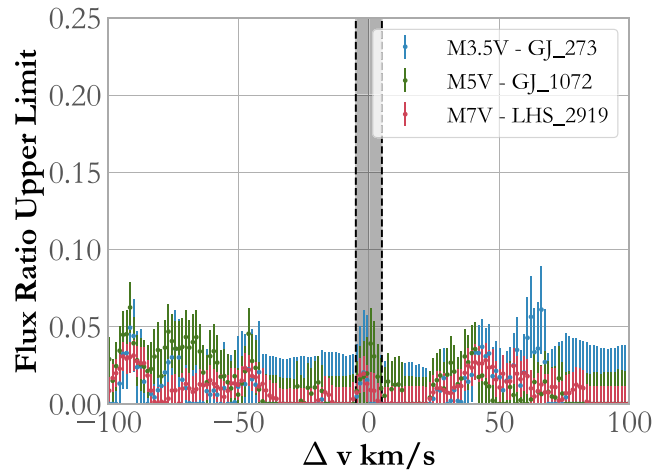
distance of $2''.67$ or a projected separation of 302 au from TOI-3714. This companion is outside both the HPF fiber ($\sim 1''.7$ on-sky; Kanodia et al. 2018) and the NEID HR fiber ($\sim 0''.9$ on-sky; Schwab et al. 2016).

To estimate the physical parameters of the white dwarf companion, we use the `WD_models`⁴¹ package from Cheng et al. (2019) to derive a photometric age and mass from its location (see Figure 11) on the Gaia color–magnitude diagram (data from Gentile Fusillo et al. 2021). We assume the atmosphere is composed of hydrogen and adopted the cooling models of Bédard et al. (2020). We adopt these colors as nominal values but note that the proximity to TOI-3714 introduces some blending and contamination in the colors of the white dwarf companion, limiting the reliability of the estimated parameters. We use the `phot_bp_rp_excess_factor` as a diagnostic to determine if any of the measured

⁴¹ https://github.com/SihaoCheng/Wd_models



(a) Flux ratio upper limits for TOI-3714.



(b) Flux ratio upper limits for TOI-3629.

Figure 10. Flux upper limits placed on the flux ratio of a secondary companion to a template spectrum as a function of Δv , obtained by fitting the wavelength region spanning $\sim 10450\text{--}10580 \text{ \AA}$ (HPF order index 17). We include the 1σ error bars, and shade the region corresponding to $\pm 5 \text{ km s}^{-1}$. We place a conservative upper limit on the flux ratio of 0.07 for an unresolved stellar companion at separations $|\Delta v| > 5 \text{ km s}^{-1}$.

blue or red Gaia photometry are problematic (Evans et al. 2018; Riello et al. 2021). We use Table 2 and Equation (6) from Riello et al. (2021) to calculate the corrected `phot_bp_rp_excess_factor`, which attempts to account for the color-dependent mean trend in this parameter. The corrected `phot_bp_rp_excess_factor` for the white dwarf companion is 0.81, and the deviation from zero suggests this object has some degree of contamination.

Without additional photometry of TIC 662037581, we provide nominal parameters to qualitatively describe the companion. The estimated mass for the white dwarf companion is $M_{WD} \sim 1.07 M_{\odot}$ with a cooling age of ~ 2.4 Gyr. The MIST semi-empirical white dwarf initial-final mass relationship from Cummings et al. (2018) suggests the progenitor star had a mass between $4.5\text{--}6.8 M_{\odot}$. Stars in this mass range have typical lifetimes (pre-main sequence through post-asymptotic giant branch) of < 0.1 Gyr (Choi et al. 2016; Dotter 2016). Assuming this object is coeval with TOI-3714, the combined progenitor lifetime and white dwarf cooling age (~ 2.4 Gyr) is consistent with the age range of $0.7\text{--}5.1$ Gyr estimated from the rotation period of TOI-3714 (23.3 ± 0.3 days).

Approximately half of all hot Jupiter systems are known to have resolved stellar companions between separations of $50\text{--}2000$ au (e.g., Knutson et al. 2014; Wang et al. 2014; Ngo et al. 2015, 2016; Marzari & Thebault 2019; Hwang et al. 2020; Fontanive & Bardalez Gagliuffi 2021), but only 14 other exoplanetary systems (see Table 2 in Martin et al. 2021) are known to have a distant white dwarf companion. Of these 14 systems, only the TOI-1259 (Martin et al. 2021) and WASP-98 (Hellier et al. 2014) systems host hot Jupiters. The existence of a distant stellar companion has been proposed as one mechanism to form hot Jupiters via a combination of secular interactions with the stellar companion and tidal friction (e.g., Fabrycky & Tremaine 2007; Anderson et al. 2016; Vick et al. 2019). Ngo et al. (2016) note that most hot Jupiters with distant stellar companions are too separated to form via this mechanism.

If the TOI-3714 system was initially a wide binary with an initial progenitor separation comparable to the observed

separation (~ 302 au), the timescale for the Kozai cycles (Equation (7) from Kiseleva et al. 1998) would be ~ 2.8 Gyr. This timescale is comparable to the age of the system and too long to effectively perturb a gas giant. The separation between the progenitor star and TOI-3714 could not have been too small, as a stellar binary with an initial separation $a \lesssim 10$ au may interact when the primary star evolves off the main sequence and common envelope effects would subsequently shrink the orbit (see Paczyński 1971; Paczynski 1976; Ivanova et al. 2013). Instead, the progenitor star could have been on a smaller orbit of tens of au and the onset of mass loss could have caused the orbit to expand (see Nordhaus et al. 2010; Nordhaus & Spiegel 2013) to the observed separation. For example, at separations of 30 au, the Kozai timescale approaches ~ 3 Myr, and it may be possible that the progenitor was close enough to perturb a nascent gas giant and far enough from TOI-3714 to prevent significant orbital decay.

Gaia EDR3 is able to place constraints on the eccentricity of resolved wide binaries (e.g., Tokovinin 2020; Hwang et al. 2022). The precision of Gaia EDR3 proper motion measurements allow for a measurement of the relative velocity for wide binaries (within the orbital plane) and allow a measurement of the angle between the separation vector and the relative velocity vector (the $v-r$ angle). This is a function of the phase, inclination, eccentricity, and argument of pericenter (see Appendix A in Hwang et al. 2022, for a detailed derivation). The measured $v-r$ angle is $169^{\circ} \pm 14^{\circ}$ and is significantly discrepant from a circular, face-on orbit ($v-r = 90^{\circ}$). We follow the methodology and use the software⁴² described in Hwang et al. (2022) to estimate the posterior of the eccentricity distribution after adopting the parameters for the best-fitting power law (Equation (29) in Hwang et al. 2022) to the wide binary sample identified by El-Badry et al. (2021). We note this eccentricity inference assumes that the wide companion has a random orbital orientation, an assumption that may not be true if the inner system is a transiting system. If the orbital orientation is not random, a large $v-r$ angle can indicate either

⁴² <https://github.com/HC-Hwang/Eccentricity-of-wide-binaries>

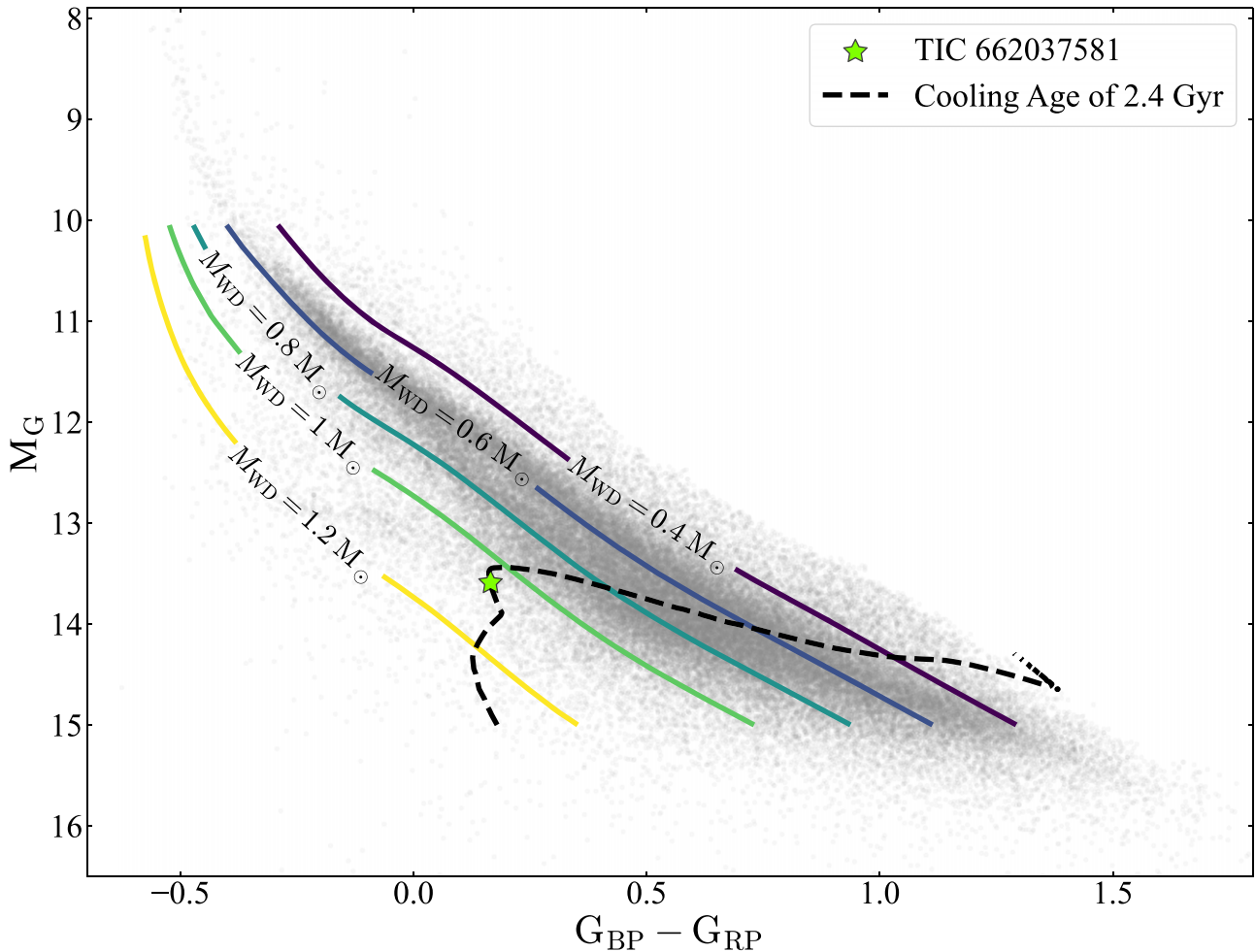


Figure 11. Nominal position of TIC 662037581, the white dwarf companion to TOI-3714, on the color–magnitude diagram for white dwarfs identified in Gaia EDR3 by Gentile Fusillo et al. (2021). Contours for fixed masses from Bédard et al. (2020) are plotted for reference. The best-matching cooling track from the models is shown with a dashed line.

a (i) high eccentricity or (ii) the outer companion lies on an orbit that is coplanar with the inner transiting system (see Appendix B in Hwang & Zakamska 2020; Behrmard et al. 2022). The inferred eccentricity with 1σ uncertainties for the orbit of the white dwarf companion is $e = 0.99^{+0.01}_{-0.47}$. The high eccentricity is consistent with the scenario in which the progenitor star was on a smaller orbit that widened and became eccentric due to mass loss. In this scenario, the resolved companion may have interacted with and impacted the migration of TOI-3714 b as it evolved into a white dwarf.

5.4. Comparison to the M Dwarf Planet Population

With the discovery of TOI-3714 b and TOI-3629 b, there are nine M dwarf systems hosting transiting hot Jupiters ($P < 10$ days and $R_p > 8R_\oplus$). Figure 12 compares the planetary mass–radius, stellar $T_e - \log g_*$, and the insolation flux of M dwarfs with transiting planets that have $R > 2R_\oplus$. Of the transiting hot Jupiters orbiting M dwarfs, TOI-3629 b has the smallest radius and mass ($\sim 0.9 R_{\text{Saturn}}$ and $\sim 0.9 M_{\text{Saturn}}$), and is the second-coolest hot Jupiter with an insolation flux of $S = 39 \pm 2 S_\oplus$. TOI-3714 has a radius comparable to the median value ($1 R_J$) and an insolation flux ($S = 54 \pm 5 S_\oplus$) comparable to the median value ($\sim 60 S_\oplus$) of the population of hot Jupiters transiting M dwarfs. TOI-3714 is, however, the

only known M dwarf with both a transiting hot Jupiter and a resolved wide companion.

All M dwarfs hosting short-period ($P < 10$ days) Jupiter-sized gas giants, including TOI-3714 b and TOI-3629 b, are early M dwarfs (M0–M3; $3400 \text{ K} < T_e < 4000 \text{ K}$). This may simply be an observational bias or a result of a small population size, but in the framework of core accretion, factors such as protoplanetary disk mass may impact the formation of gas giants (e.g., Mordasini et al. 2012; Hasegawa & Pudritz 2013, 2014; Adibekyan 2019). M dwarf protoplanetary disks have lower masses than the disks around Sun-like stars (e.g., Andrews et al. 2013; Mohanty et al. 2013; Stamatellos & Herczeg 2015; Ansdell et al. 2017); disk masses for these stars are typically below a few Jupiter masses (Ansdell et al. 2017; Manara et al. 2018), such that the efficiency of gas giant formation is expected to increase when orbiting more massive M dwarfs because the materials that form gas giant cores are more abundant compared to the low-mass protoplanetary disks around later M dwarfs.

In addition to the protoplanetary disk mass, the stellar metallicity has been known to be important for gas giant formation. The planet–metallicity correlation, in which metal-rich stars are more likely to host gas giant planets, has been extensively observed in Sun-like stars (e.g., Fischer & Valenti 2005; Johnson et al. 2010; Guo et al. 2017; Osborn &

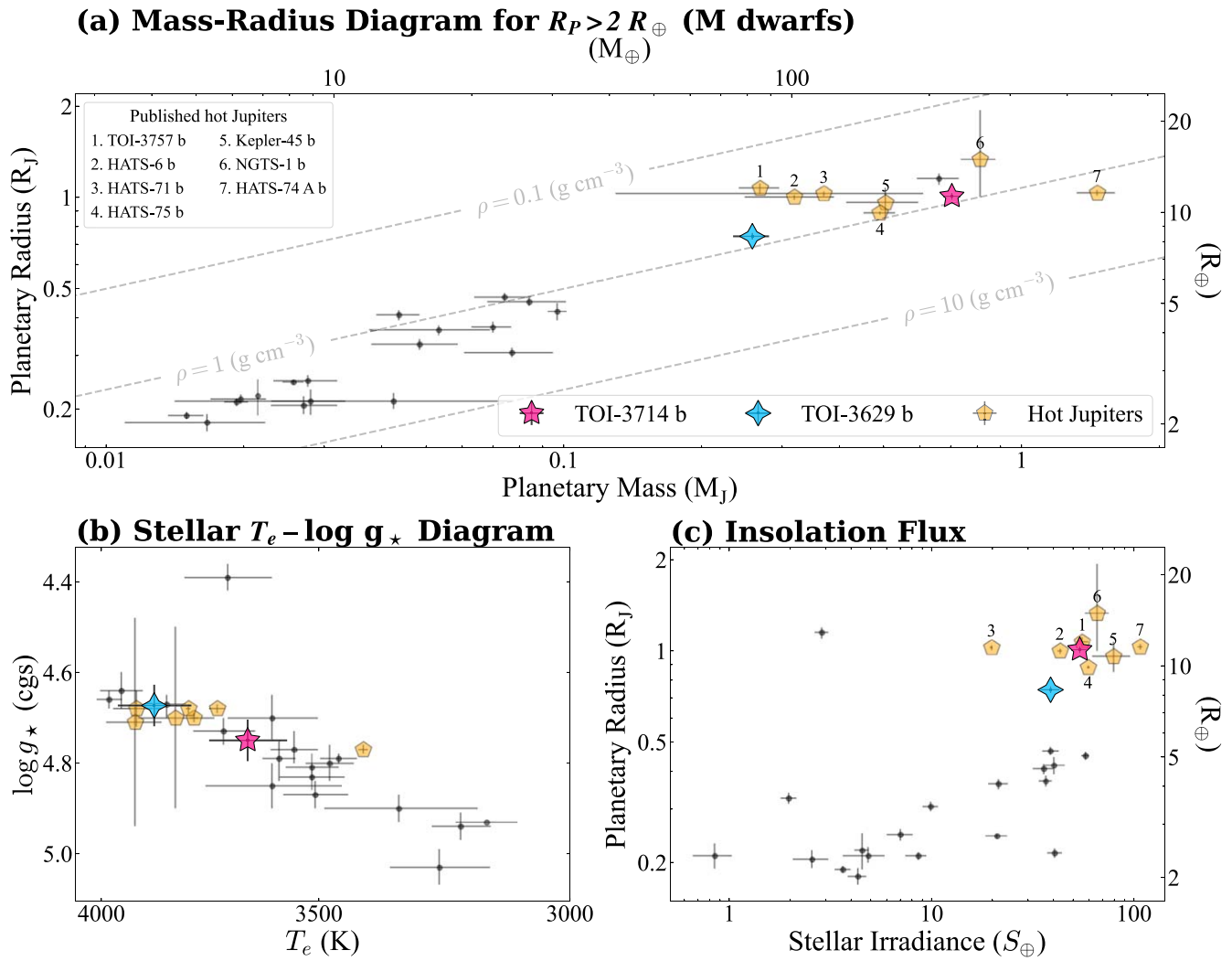


Figure 12. Physical parameters of the TOI-3714 and TOI-3629 systems. (a) Positions of TOI-3714 b (star) and TOI-3629 b (diamond star) on the mass–radius diagram for transiting M dwarf exoplanets with mass measurements and $R_p > 2 R_{\oplus}$. All previously known hot Jupiters ($P < 10$ days and $R_p \geq 8 R_{\oplus}$) transiting M dwarfs are marked as pentagons with numbers linked to the planet name. Contours of fixed bulk density are plotted for reference. (b) Positions of TOI-3714 and TOI-3629 on an effective temperature–surface gravity diagram. (c) Insolation flux for M dwarf exoplanets. The data were compiled from the [NASA Exoplanet Archive](#) (Akeson et al. 2013) on 2022 May 4.

Bayliss 2020). RV studies (e.g., Neves et al. 2013; Maldonado et al. 2020) have suggested that the planet–metallicity correlation exists for M dwarfs but there is no statistical study for M dwarfs with transiting gas giants because of the small population size. Figure 13 compares the metallicity and planetary radii of these two systems with transiting exoplanets from the NASA Exoplanet Archive. All M dwarfs hosting a transiting Jupiter-sized planet ($R \geq 8 R_{\oplus}$), including TOI-3714 and TOI-3629, have metallicities of $[\text{Fe}/\text{H}] > 0$. We perform a simple binomial probability calculation to assess how likely it is that all 10 Jupiter-sized companions are found to have $[\text{Fe}/\text{H}] \geq 0$ by random chance. If we assume a uniform distribution in metallicity between the range of $-0.5 < [\text{Fe}/\text{H}] < 0.5$, the probability that all nine M dwarfs hosting hot Jupiters fall within the observed range of $[\text{Fe}/\text{H}] \geq 0$ is $\sim 0.2\%$.

We note that the metallicities on the NASA Exoplanet Archive are also not homogeneously derived. Metallicities derived using different techniques or instruments may exhibit offsets (e.g., Guo et al. 2017; Petigura et al. 2018). A magnitude limited search from a nontargeted transit survey, such as TESS,

to identify a population of hot Jupiters orbiting M dwarfs is required to statistically evaluate if the planet–metallicity and stellar mass correlations apply to the population of transiting M dwarf gas giants. TESS is an ideal mission for this study, as it has been shown to be complete for hot Jupiters transiting earlier Sun-like stars (Zhou et al. 2019) and it should detect almost all transiting hot Jupiter–M dwarf systems given the large transit depth. This population of hot Jupiters could then be extensively studied to provide statistical constraints on the existence and strength of correlations of gas giant planets with metallicity or stellar mass.

TOI-3714 and TOI-3629, like the six existing M dwarf systems with transiting hot Jupiters, also lack additional transiting planets on nearby orbits. We search for additional transiting companions in the TESS data for each system by using the transit least-squares algorithm (TLS; Hippke & Heller 2019) after subtracting the best-fitting transit model for each planet. For both TOI-3714 and TOI-3629, TLS only identifies candidate signals (depths > 1 ppm) between 1 and 13 days where the test statistic is below the suggested value of 7.

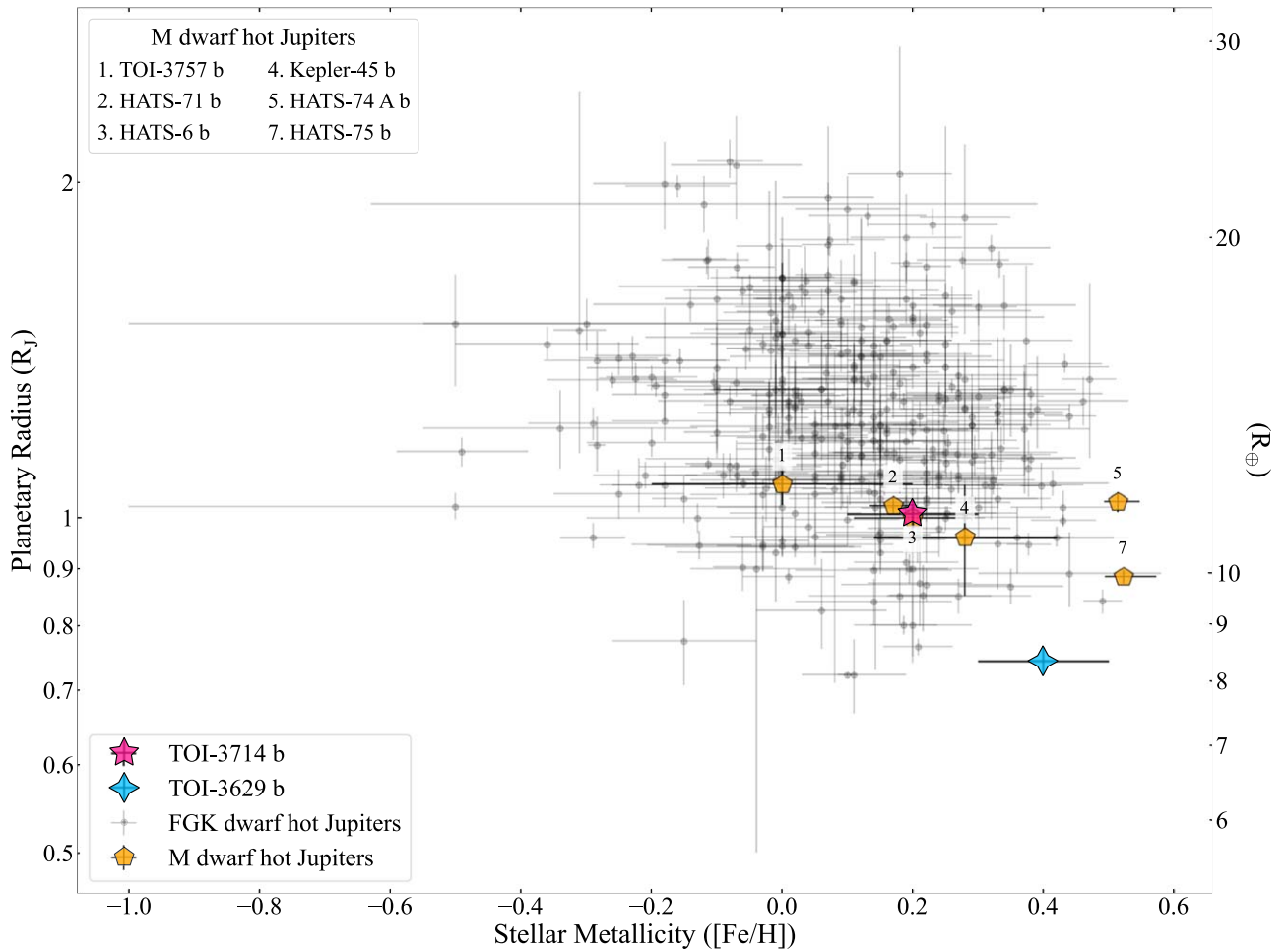


Figure 13. Positions of TOI-3714 and TOI-3629 on a metallicity–mass diagram for transiting hot Jupiters ($R \geq 8 R_{\oplus}$ and $P < 10$ days). All known hot Jupiters transiting M dwarfs have $[\text{Fe}/\text{H}] > 0$. The same numbers from Figure 12 are included to identify the M-dwarf hot Jupiters. HATS-6 b is behind the marker for TOI-3714 b. NGTS-1 b lacks a metallicity measurement (Bayliss et al. 2018) and is not plotted. The data were compiled from the [NASA Exoplanet Archive](#) on 2022 May 04.

This threshold corresponds to a false-positive rate of $\sim 1\%$ for the TLS algorithm. The maximum radius of a candidate signal identified by TLS was $\sim 4 M_{\oplus}$ and $\sim 5 M_{\oplus}$ for TOI-3714 and TOI-3629, respectively, such that the current TESS data excludes the existence of additional transiting gas giant companions in the TESS data.

Only five transiting hot Jupiters are known to exist in compact multiplanet systems: WASP-47 b (Becker et al. 2015), Kepler-730 b (Zhu et al. 2018; Cañas et al. 2019), TOI-1130c (Huang et al. 2020c), WASP-148 b (Wang et al. 2022), and WASP-132 b (Hord et al. 2022). This apparent low planetary multiplicity rate for hot Jupiters orbiting Sun-like stars has been detected in the analysis of multiple statistical samples from ground and space-based transiting hot Jupiters (e.g., Steffen et al. 2012; Huang et al. 2016; Maciejewski 2020; Hord et al. 2021; Wang et al. 2021; Zhu & Dong 2021). The apparent lack of close-period companions to hot Jupiters may be imprints of high-eccentricity migration (e.g., Mustill et al. 2015; Dawson & Johnson 2018), as this mechanism would destabilize shorter period planets. TOI-3714 and TOI-3629 will both be observed in TESS cycle 5 and both sectors of data for each target could be analyzed in detail (e.g., similar to Hord et al. 2021) to provide robust constraints on additional transiting companions.

5.5. Comparison to Planetary Models

The equilibrium temperatures of TOI-3714 b ($T_{\text{eq}} = 750 \pm 20$ K) and TOI-3629 b ($T_{\text{eq}} = 690 \pm 20$ K) are < 1000 K, and it is unlikely these planets exhibit radius inflation due to stellar flux-driven mechanisms. Studies of the population of Kepler hot Jupiters (e.g., Demory & Seager 2011) determined that gas giants receiving an incident flux $\lesssim 2 \times 10^8 \text{ erg s}^{-1} \text{ cm}^{-2}$ have radii that are independent of the stellar incident flux. More recent analyses on transiting hot Jupiters (e.g., Thorngren & Fortney 2018; Thorngren et al. 2021) have confirmed that inflated radii are evident in the population of hot Jupiters with $T_{\text{eq}} > 1000$ K serving as a threshold for the onset of ohmic heating and planetary inflation (e.g., Batygin & Stevenson 2010; Batygin et al. 2011; Miller & Fortney 2011).

Both the hot Jupiters TOI-3714 b and TOI-3629 b have $T_{\text{eq}} < 1000$ K and do not show anomalously large radii when compared to models for gas giants from Baraffe et al. (2008) and Fortney et al. (2007). The models from Fortney et al. (2007) assume a solar metallicity hydrogen and helium atmosphere with a heavy element core that is composed of a 50–50 mixture of ice (water) and rock (olivine) while the models from Baraffe et al. (2008) assume a gaseous hydrogen and helium envelope with a distribution of heavy elements

(water, dunite, and iron). Although these models are generated for the population of hot Jupiters transiting Sun-like stars, both TOI-3714 and TOI-3629 are in agreement with the nonirradiated models for gas giant interiors. We compared the observed radii of TOI-3714 b and TOI-3629 b to the radius predicted between 1 and 7 Gyr models for a solar metallicity atmosphere and note agreement within $2\text{--}3\sigma$ regardless of age. The mass and radius of TOI-3714 b are in agreement with the models from Baraffe et al. (2008) containing a small fraction of heavy metals ($\sim 2\%$) and with the Fortney et al. (2007) models for a core mass of 2%–4% of the planetary mass. The mass and radius of TOI-3629 are consistent with models from Fortney et al. (2007) having a core mass $\sim 30\%$ of the planetary mass or the Baraffe et al. (2008) models with a heavy metal fraction of $\sim 20\%$ – 40% . These heavy metal fractions are consistent with what is seen in Jupiter ($<10\%$ core mass; Wahl et al. 2017) and Saturn ($\sim 20\%$; Mankovich & Fuller 2021) in the solar system.

5.6. Future Characterization

5.6.1. Stellar Obliquity

The projected stellar obliquity (λ) is the apparent angle between the stellar rotation axis and the normal to the planet of the orbit. It can shed light on the dynamical and formation history of planets (e.g., Albrecht et al. 2012; Winn & Fabrycky 2015; Triaud 2018; Albrecht et al. 2021). Measurements of λ for hot Jupiters orbiting Sun-like stars (e.g., Albrecht et al. 2012; Dawson 2014) have revealed an obliquity distribution that is consistent with tidal realignment, indicating that their origin channels most likely involve dynamical interactions, such as planet–planet scattering. To date, there is no measurement of λ for any M dwarf hosting a hot Jupiter. The measurement of λ for either system via the Rossiter–McLaughlin (RM) effect (Triaud 2018) could limit the physical processes involved during formation because some mechanisms, such as disk migration, prohibit highly misaligned orbits (see Dawson & Johnson 2018).

The amplitude of the RM effect can be estimated as $\Delta V = 2/3(R_p/R_*)^2 v \sin i_* \sqrt{1 - b^2}$ (Equation (1); Triaud 2018). For TOI-3714, we estimate an equatorial ($\sin i = 1$) rotational velocity of $v_{\text{eq}} = 1.08 \pm 0.06 \text{ km s}^{-1}$ using the derived rotation period and stellar radius. Additional photometric observations of TOI-3629 are required to determine the rotation period; however, if we adopt a value of $P_{\text{rot}} = 30$ days corresponding to the marginally significant peak seen in its ZTF zr data, the equatorial rotational velocity would be $v_{\text{eq}} = 1 \text{ km s}^{-1}$. We use the derived transit parameters to estimate the RM effect amplitudes as $\sim 30 \text{ m s}^{-1}$ and $\sim 10 \text{ m s}^{-1}$ for TOI-3714 and TOI-3629, respectively. The precision to detect these amplitudes can be achieved using current high-resolution spectrographs with extended red wavelength coverage because both of these targets are early M dwarfs with a peak in the SED at around $\sim 0.8\text{--}0.9 \mu\text{m}$.

5.6.2. Transmission Spectroscopy

TOI-3714 and TOI-3629 are the two brightest M dwarfs ($J < 12$) with a transiting hot Jupiter and are potential targets to probe the atmosphere of warm ($T_{\text{eq}} \sim 700 \text{ K}$) M dwarf—hot Jupiter systems. Sing et al. (2016) obtained transmission spectra of hot Jupiters transiting Sun-like stars and noticed the observed sample contained both cloudy and clear planets, suggesting that hot Jupiters did not exhibit a strong relationship

to cloud formation. While no extensive studies have been performed on M-dwarf hot Jupiters, the transmission spectroscopy metric (TSM; Kempton et al. 2018) suggests that both TOI-3714 b (TSM = 98 ± 7) and TOI-3629 b (TSM = 80 ± 9) are amenable to observations with the James Webb Space Telescope (JWST; Gardner et al. 2006). These systems also have the precision on mass and radius (both determined at $>10\sigma$) needed for detailed atmospheric analysis (Batalha et al. 2019). It may be possible to determine atmospheric abundances of C-, N-, and O-bearing molecules in the atmospheres of these planets to probe the thermal structure of the interior (Fortney et al. 2020). While these hot Jupiters do not have the highest TSM of the existing population (TOI-3757 has the highest TSM of 180 ± 30), they are unique in the population as TOI-3629 b is the smallest hot Jupiter orbiting an M dwarf while TOI-3714 is one of the coolest M dwarfs hosting a hot Jupiter.

TOI-3714 and TOI-3629 provide an opportunity to examine the prevalence of clouds and photochemical hazes for M dwarf exoplanets. Under certain combinations of temperature and surface gravity, clouds or hazes may form in the visible region of a hot Jupiter atmosphere either through condensation chemistry or photochemical processes (e.g., Sudarsky et al. 2003; Helling et al. 2008; Marley et al. 2013), and the presence of clouds or hazes may weaken or mask spectral features (Sing et al. 2016; Sing 2018). Photochemical processes are more efficient in cooler exoplanets (e.g., Moses et al. 2011) and high-incident stellar UV irradiation is thought to enhance the photochemical production of hydrocarbon aerosols (e.g., Liang et al. 2004; Line et al. 2010). Transmission spectra of TOI-3714 b and TOI-3629 b with the JWST would probe atmospheric chemistry of gas giants orbiting M dwarfs and the effects of higher UV radiation environment of early M dwarfs on atmospheric chemistry (e.g., Pineda et al. 2021).

6. Summary

We report the discovery of two gas giants orbiting M dwarfs. TOI-3714 b is a hot Jupiter ($M_p = 0.70 \pm 0.03 M_J$ and $R_p = 1.01 \pm 0.03 R_J$) on a $P = 2.154849 \pm 0.000001$ day orbit. TOI-3629 b is a hot Jupiter ($M_p = 0.26 \pm 0.02 M_J$ and $R_p = 0.74 \pm 0.02 R_J$) on a $P = 3.936551^{+0.000005}_{-0.000006}$ day orbit. Only TOI-3714 has a detectable rotation period of 23.3 ± 0.3 days and most probably has an age between 0.7 and 5.1 Gyr, which is comparable to the nominal cooling age of its white dwarf companion (~ 2.4 Gyr). All hot Jupiters known to transit M dwarfs, including TOI-3714 and TOI-3629, orbit metal-rich early M dwarfs (M0–M3). A larger population size and homogeneously derived metallicities are required to confirm if the correlations with metallicity and stellar mass observed for hot Jupiters orbiting Sun-like stars are also observed in the population of M dwarf gas giants. Constraints from Gaia EDR3 and RVs reject the presence of massive short-period companions to both gas giants, but TOI-3714 has a resolved white dwarf companion at a projected separation of $\sim 300 \text{ au}$ and most likely on an eccentric orbit. The progenitor may have been close enough to impact the orbit of a nascent TOI-3714 b as it evolved into a white dwarf. TOI-3714 and TOI-3629 are the brightest M dwarfs hosting hot Jupiters ($J < 12$) and are amenable to observations during transit to (i) further our understanding of their dynamical history with a measurement of the projected obliquity and (ii) explore the atmospheric chemistry of hot gas giants orbiting cool stars.

The Pennsylvania State University campuses are located on the original homelands of the Erie, Haudenosaunee (Seneca, Cayuga, Onondaga, Oneida, Mohawk, and Tuscarora), Lenape (Delaware Nation, Delaware Tribe, Stockbridge-Munsee), Shawnee (Absentee, Eastern, and Oklahoma), Susquehannock, and Wahzhazhe (Osage) Nations. As a land grant institution, we acknowledge and honor the traditional caretakers of these lands and strive to understand and model their responsible stewardship. We also acknowledge the longer history of these lands and our place in that history.

We acknowledge support from NSF grants AST 1006676, AST 1126413, AST 1310875, AST 1310885, AST 2009554, AST 2009889, AST 2108512 and the NASA Astrobiology Institute (NNA09DA76A) in our pursuit of precision RVs in the near-infrared. We acknowledge support from the Heising-Simons Foundation via grant 2017-0494. We acknowledge support from NSF grants AST 1907622, AST 1909506, AST 1909682, AST 1910954 and the Research Corporation in connection with precision diffuser-assisted photometry.

This work is Contribution 0046 from the Center for Planetary Systems Habitability at the University of Texas at Austin. These results are based on observations obtained with HPF on the HET. The HET is a joint project of the University of Texas at Austin, the Pennsylvania State University, Ludwig-Maximilians-Universität München, and Georg-August Universität Göttingen. The HET is named in honor of its principal benefactors, William P. Hobby and Robert E. Eberly. The HET collaboration acknowledges the support and resources from the Texas Advanced Computing Center. We are grateful to the HET Resident Astronomers and Telescope Operators for their valuable assistance in gathering our HPF data. We would like to acknowledge that the HET is built on Indigenous land. Moreover, we would like to acknowledge and pay our respects to the Carrizo & Comecrudo, Coahuiltecan, Caddo, Tonkawa, Comanche, Lipan Apache, Alabama-Coushatta, Kickapoo, Tigua Pueblo, and all the American Indian and Indigenous Peoples and communities who have been or have become a part of these lands and territories in Texas, here on Turtle Island.

Some of the data presented were obtained by the NEID spectrograph built by the Pennsylvania State University and operated at the WIYN Observatory by NOIRLab, which is managed by the Association of Universities for Research in Astronomy (AURA) under a cooperative agreement with the NSF, and operated under the NN-EXPLORE partnership of NASA and the NSF. Observations with NEID were obtained under proposals 2021B-0035 (PI: S. Kanodia), 2021B-0435 (PI: S. Kanodia), and 2021B-0438 (PI: C. Canas). NEID results included here utilize the Data Reduction Pipeline operated by NExScI and developed under subcontract 1644767 between JPL and the University of Arizona. This work was performed for the Jet Propulsion Laboratory, California Institute of Technology, sponsored by the United States Government under the Prime Contract 80NM0018D0004 between Caltech and NASA. WIYN is a joint facility of the University of Wisconsin-Madison, Indiana University, NSF's NOIRLab, the Pennsylvania State University, Purdue University, University of California-Irvine, and the University of Missouri. The authors are honored to be permitted to conduct astronomical research on Iolkam Du'ag (Kitt Peak), a mountain with particular significance to the Tohono O'odham.

Some of results are based on observations obtained with the Apache Point Observatory 3.5 m telescope, which is owned

and operated by the Astrophysical Research Consortium. We wish to thank the APO 3.5 m telescope operators in their assistance in obtaining these data.

Some of the observations in this paper made use of the NN-EXPLORE Exoplanet and Stellar Speckle Imager (NESSI). NESSI was funded by the NASA Exoplanet Exploration Program and the NASA Ames Research Center. NESSI was built at the Ames Research Center by Steve B. Howell, Nic Scott, Elliott P. Horch, and Emmett Quigley.

Some of the data presented in this paper were obtained from MAST at STScI. Support for MAST for non-HST data is provided by the NASA Office of Space Science via grant NNX09AF08G and by other grants and contracts. This work includes data collected by the TESS mission, which are publicly available from MAST. Funding for the TESS mission is provided by the NASA Science Mission directorate. This research made use of the (i) NASA Exoplanet Archive, which is operated by Caltech, under contract with NASA under the Exoplanet Exploration Program, (ii) SIMBAD database, operated at CDS, Strasbourg, France, (iii) NASA's Astrophysics Data System Bibliographic Services, (iv) NASA/IPAC Infrared Science Archive, which is funded by NASA and operated by the California Institute of Technology, and (v) data from 2MASS, a joint project of the University of Massachusetts and IPAC at Caltech, funded by NASA and the NSF.

This work has made use of data from the European Space Agency (ESA) mission Gaia (<https://www.cosmos.esa.int/gaia>), processed by the Gaia Data Processing and Analysis Consortium (DPAC; <https://www.cosmos.esa.int/web/gaia/dpac/consortium>). Funding for the DPAC has been provided by national institutions, in particular the institutions participating in the Gaia Multilateral Agreement.

Some of the observations in this paper made use of the Guoshoujing Telescope (LAMOST), a National Major Scientific Project built by the Chinese Academy of Sciences. Funding for the project has been provided by the National Development and Reform Commission. LAMOST is operated and managed by the National Astronomical Observatories, Chinese Academy of Sciences.

Some of the observations in this paper were obtained with the Samuel Oschin Telescope 48 inch and the 60 inch Telescope at the Palomar Observatory as part of the ZTF project. Z.T.F. is supported by the NSF under grant No. AST-2034437 and a collaboration including Caltech, IPAC, the Weizmann Institute for Science, the Oskar Klein Center at Stockholm University, the University of Maryland, Deutsches Elektronen-Synchrotron and Humboldt University, the TANGO Consortium of Taiwan, the University of Wisconsin at Milwaukee, Trinity College Dublin, Lawrence Livermore National Laboratories, and IN2P3, France. Operations are conducted by COO, IPAC, and UW. We thank the anonymous referee for valuable feedback, which has improved the quality of this manuscript. We thank Kareem El-Badry and David V. Martin for useful discussions. C.I.C. acknowledges support by NASA Headquarters under the NASA Earth and Space Science Fellowship Program through grant 80NSSC18K1114, the Alfred P. Sloan Foundation's Minority Ph.D. Program through grant G-2016-20166039, and the Pennsylvania State University's Bunton-Waller program. The Center for Exoplanets and Habitable Worlds is supported by the Pennsylvania State University and the Eberly College of Science. The computations for this research were performed on the Pennsylvania State University's Institute for







Computational and Data Sciences' Roar supercomputer, including the CyberLAMP cluster supported by NSF grant MRI-1626251. This content is solely the responsibility of the authors and does not necessarily represent the views of the Institute for Computational and Data Sciences. H.C.H. acknowledges the support of the Infosys Membership at the Institute for Advanced Study. T.N.S. acknowledges support from the Wyoming Research Scholars Program.

Facilities: ARC (ARCTIC), Exoplanet Archive, Gaia, HET (HPF), IRSA, KPNO:2.1 m (Robo-AO), LAMOST, MAST, PO:1.2 m (ZTF), PO:1.5 m (ZTF), SO:Kuiiper, TESS, WIYN (NEID, NESSI).

Software: astroquery (Ginsburg et al. 2019), astropy (Astropy Collaboration et al. 2018), barycorrpy (Kanodia & Wright 2018), dynesty (Speagle 2020), EXOFASTv2 (Eastman et al. 2019), GLS (Zechmeister & Kürster 2009), HPF-SpecMatch (S. Jones et al. 2022), juliet (Espinoza et al. 2019), lightkurve (Lightkurve Collaboration et al. 2018), matplotlib (Hunter 2007), numpy (van der Walt et al. 2011), pandas (McKinney 2010), scipy (Virtanen et al. 2020), telfit (Gullikson et al. 2014), thejoker (Price-Whelan et al. 2017), TLS (Hippke & Heller 2019), WD_models (Cheng et al. 2019).

ORCID iDs

Caleb I. Cañas  <https://orcid.org/0000-0003-4835-0619>
 Shubham Kanodia  <https://orcid.org/0000-0001-8401-4300>
 Chad F. Bender  <https://orcid.org/0000-0003-4384-7220>
 Suvrath Mahadevan  <https://orcid.org/0000-0001-9596-7983>
 Gudmundur Stefánsson  <https://orcid.org/0000-0001-7409-5688>
 William D. Cochran  <https://orcid.org/0000-0001-9662-3496>
 Andrea S. J. Lin  <https://orcid.org/0000-0002-9082-6337>
 Hsiang-Chih Hwang  <https://orcid.org/0000-0003-4250-4437>
 Luke Powers  <https://orcid.org/0000-0002-5300-5353>
 Andrew Monson  <https://orcid.org/0000-0002-0048-2586>
 Elizabeth M. Green  <https://orcid.org/0000-0003-3688-2298>
 Brock A. Parker  <https://orcid.org/0000-0001-9307-8170>
 Tera N. Swaby  <https://orcid.org/0000-0002-5817-202X>
 Henry A. Kobulnicky  <https://orcid.org/0000-0002-4475-4176>
 John Wisniewski  <https://orcid.org/0000-0001-9209-1808>
 Arvind F. Gupta  <https://orcid.org/0000-0002-5463-9980>
 Mark E. Everett  <https://orcid.org/0000-0002-0885-7215>
 Sinclair Jones  <https://orcid.org/0000-0002-7227-2334>
 Benjamin Anjakos  <https://orcid.org/0000-0001-7614-9205>
 Corey Beard  <https://orcid.org/0000-0001-7708-2364>
 Cullen H. Blake  <https://orcid.org/0000-0002-6096-1749>
 Scott A. Diddams  <https://orcid.org/0000-0002-2144-0764>
 Connor Fredrick  <https://orcid.org/0000-0002-0560-1433>
 Elnaz Hakemiamjad  <https://orcid.org/0000-0003-0112-9095>
 Leslie Hebb  <https://orcid.org/0000-0003-1263-8637>
 Jessica E. Libby-Roberts  <https://orcid.org/0000-0002-2990-7613>
 Sarah E. Logsdon  <https://orcid.org/0000-0002-9632-9382>
 Michael W. McElwain  <https://orcid.org/0000-0003-0241-8956>
 Andrew J. Metcalf  <https://orcid.org/0000-0001-5000-1018>
 Joe P. Ninan  <https://orcid.org/0000-0001-8720-5612>

Jayadev Rajagopal  <https://orcid.org/0000-0002-2488-7123>
 Lawrence W. Ramsey  <https://orcid.org/0000-0002-4289-7958>
 Paul Robertson  <https://orcid.org/0000-0003-0149-9678>
 Arpita Roy  <https://orcid.org/0000-0001-8127-5775>
 Jacob Rühle  <https://orcid.org/0000-0003-1082-9720>
 Christian Schwab  <https://orcid.org/0000-0002-0091-7105>
 Ryan C. Terrien  <https://orcid.org/0000-0002-4788-8858>
 Jason T. Wright  <https://orcid.org/0000-0001-6160-5888>

References

- Adibekyan, V. 2019, *Geosc*, 9, 105
 Akeson, R. L., Chen, X., Ciardi, D., et al. 2013, *PASP*, 125, 989
 Albrecht, S., Winn, J. N., Johnson, J. A., et al. 2012, *ApJ*, 757, 18
 Albrecht, S. H., Marcussen, M. L., Winn, J. N., Dawson, R. I., & Knudstrup, E. 2021, *ApJL*, 916, L1
 Anderson, K. R., Storch, N. I., & Lai, D. 2016, *MNRAS*, 456, 3671
 Andrews, S. M., Rosenfeld, K. A., Kraus, A. L., & Wilner, D. J. 2013, *ApJ*, 771, 129
 Anglada-Escudé, G., & Butler, R. P. 2012, *ApJS*, 200, 15
 Angus, R., Morton, T., Aigrain, S., Foreman-Mackey, D., & Rajpaul, V. 2018, *MNRAS*, 474, 2094
 Ansdell, M., Williams, J. P., Manara, C. F., et al. 2017, *AJ*, 153, 240
 Astropy Collaboration, Price-Whelan, A. M., Sipőcz, B. M., et al. 2018, *AJ*, 156, 123
 Bailer-Jones, C. A. L., Rybizki, J., Fousneau, M., Demleitner, M., & Andrae, R. 2021, *AJ*, 161, 147
 Bakos, G. Á., Bayliss, D., Bento, J., et al. 2020, *AJ*, 159, 267
 Baraffe, I., Chabrier, G., & Barman, T. 2008, *A&A*, 482, 315
 Baranec, C., Riddle, R., Law, N. M., et al. 2013, *JVE*, 72, 50021
 Baranec, C., Riddle, R., Law, N. M., et al. 2014, *ApJL*, 790, L8
 Batalha, N. E., Lewis, T., Fortney, J. J., et al. 2019, *ApJL*, 885, L25
 Batygin, K., Bodenheimer, P. H., & Laughlin, G. P. 2016, *ApJ*, 829, 114
 Batygin, K., & Stevenson, D. J. 2010, *ApJL*, 714, L238
 Batygin, K., Stevenson, D. J., & Bodenheimer, P. H. 2011, *ApJ*, 738, 1
 Bayliss, D., Gillen, E., Eigmüller, P., et al. 2018, *MNRAS*, 475, 4467
 Becker, J. C., Vanderburg, A., Adams, F. C., Rappaport, S. A., & Schwengeler, H. M. 2015, *ApJL*, 812, L18
 Bédard, A., Bergeron, P., Brassard, P., & Fontaine, G. 2020, *ApJ*, 901, 93
 Behrard, A., Dai, F., & Howard, A. W. 2022, *AJ*, 163, 160
 Belokurov, V., Penoyre, Z., Oh, S., et al. 2020, *MNRAS*, 496, 1922
 Bensby, T., Feltzing, S., & Lundström, I. 2003, *A&A*, 410, 527
 Bessell, M. S. 1990, *PASP*, 102, 1181
 Boley, A. C., Granados Contreras, A. P., & Gladman, B. 2016, *ApJL*, 817, L17
 Bonfils, X., Delfosse, X., Udry, S., et al. 2013, *A&A*, 549, A109
 Bonomo, A. S., Desidera, S., Benatti, S., et al. 2017, *A&A*, 602, A107
 Bovy, J. 2015, *ApJS*, 216, 29
 Brasseur, C. E., Phillip, C., Fleming, S. W., Mullally, S. E., & White, R. L. 2019, *Astrophysics Tools for Creating Cutouts of TESS Images*, Astrophysics Source Code Library, ascl:1905.007
 Cañas, C. I., Wang, S., Mahadevan, S., et al. 2019, *ApJL*, 870, L17
 Cañas, C. I., Stefánsson, G., Kanodia, S., et al. 2020, *AJ*, 160, 147
 Canto Martins, B. L., Gomes, R. L., Messias, Y. S., et al. 2020, *ApJS*, 250, 20
 Cheng, S., Cummings, J. D., & Ménard, B. 2019, *ApJ*, 886, 100
 Choi, J., Dotter, A., Conroy, C., et al. 2016, *ApJ*, 823, 102
 Collins, K. A., Kielkopf, J. F., Stassun, K. G., & Hessman, F. V. 2017, *AJ*, 153, 77
 Cui, X.-Q., Zhao, Y.-H., Chu, Y.-Q., et al. 2012, *RAA*, 12, 1197
 Cumming, A., Butler, R. P., Marcy, G. W., et al. 2008, *PASP*, 120, 531
 Cummings, J. D., Kalirai, J. S., Tremblay, P. E., Ramirez-Ruiz, E., & Choi, J. 2018, *ApJ*, 866, 21
 Cutri, R. M., Skrutskie, M. F., van Dyk, S., et al. 2003, *yCat*, II, 246
 Dawson, R. I. 2014, *ApJL*, 790, L31
 Dawson, R. I., & Johnson, J. A. 2018, *ARA&A*, 56, 175
 Demory, B.-O., & Seager, S. 2011, *ApJS*, 197, 12
 Dotter, A. 2016, *ApJS*, 222, 8
 Dressing, C. D., & Charbonneau, D. 2015, *ApJ*, 807, 45
 Eastman, J. D., Rodriguez, J. E., Agol, E., et al. 2019, arXiv:1907.09480
 El-Badry, K., & Rix, H.-W. 2018, *MNRAS*, 480, 4884
 El-Badry, K., Rix, H.-W., & Heintz, T. M. 2021, *MNRAS*, 506, 2269
 Endl, M., Cochran, W. D., Kürster, M., et al. 2006, *ApJ*, 649, 436
 Engle, S. G., & Guinan, E. F. 2018, *RNAAS*, 2, 34
 Espinoza, N., Kossakowski, D., & Brahm, R. 2019, *MNRAS*, 490, 2262
 Evans, D. W., Riello, M., De Angeli, F., et al. 2018, *A&A*, 616, A4

- Fabrycky, D., & Tremaine, S. 2007, *ApJ*, **669**, 1298
- Feinstein, A. D., Montet, B. T., Foreman-Mackey, D., et al. 2019, *PASP*, **131**, 094502
- Fischer, D. A., & Valenti, J. 2005, *ApJ*, **622**, 1102
- Fitzpatrick, E. L. 1999, *PASP*, **111**, 63
- Fontanive, C., & Bardalez Gagliuffi, D. 2021, *FrASS*, **8**, 16
- Ford, E. B., & Rasio, F. A. 2008, *ApJ*, **686**, 621
- Foreman-Mackey, D., Agol, E., Ambikasaran, S., & Angus, R. 2017, *AJ*, **154**, 220
- Fortney, J. J., Marley, M. S., & Barnes, J. W. 2007, *ApJ*, **659**, 1661
- Fortney, J. J., Visscher, C., Marley, M. S., et al. 2020, *AJ*, **160**, 288
- Fulton, B. J., Petigura, E. A., Blunt, S., & Sinukoff, E. 2018, *PASP*, **130**, 044504
- Gagné, J., Mamajek, E. E., Malo, L., et al. 2018, *ApJ*, **856**, 23
- Gaia Collaboration, Brown, A. G. A., Vallenari, A., et al. 2021, *A&A*, **649**, A1
- Gallet, F., Bolmont, E., Mathis, S., Charbonnel, C., & Amard, L. 2017, *A&A*, **604**, A112
- Gandhi, P., Buckley, D. A. H., Charles, P., et al. 2020, arXiv:2009.07277
- Gandolfi, D., Barragán, O., Livingston, J. H., et al. 2018, *A&A*, **619**, L10
- Gardner, J. P., Mather, J. C., Clampin, M., et al. 2006, *SSRv*, **123**, 485
- Gentile Fusillo, N. P., Tremblay, P. E., Cukanovaite, E., et al. 2021, *MNRAS*, **508**, 3877
- Gilliland, R. L., Chaplin, W. J., Jenkins, J. M., Ramsey, L. W., & Smith, J. C. 2015, *AJ*, **150**, 133
- Ginsburg, A., Sipőcz, B. M., Brasseur, C. E., et al. 2019, *AJ*, **157**, 98
- Goldreich, P., & Soter, S. 1966, *Icar*, **5**, 375
- Green, G. M., Schlafly, E., Zucker, C., Speagle, J. S., & Finkbeiner, D. 2019, *ApJ*, **887**, 93
- Gullikson, K., Dodson-Robinson, S., & Kraus, A. 2014, *AJ*, **148**, 53
- Guo, X., Johnson, J. A., Mann, A. W., et al. 2017, *ApJ*, **838**, 25
- Halverson, S., Terrien, R., Mahadevan, S., et al. 2016, *Proc. SPIE*, **9908**, 99086P
- Hardegree-Ullman, K. K., Cushing, M. C., Muirhead, P. S., & Christiansen, J. L. 2019, *AJ*, **158**, 75
- Hartman, J. D., Bayliss, D., Brahm, R., et al. 2015, *AJ*, **149**, 166
- Hasegawa, Y., & Pudritz, R. E. 2013, *ApJ*, **778**, 78
- Hasegawa, Y., & Pudritz, R. E. 2014, *ApJ*, **794**, 25
- Hedges, C., Angus, R., Barentsen, G., et al. 2020, *RNAAS*, **4**, 220
- Heller, C., Anderson, D. R., Collier Cameron, A., et al. 2014, *MNRAS*, **440**, 1982
- Helling, C., Woitke, P., & Thi, W. F. 2008, *A&A*, **485**, 547
- Henden, A. A., Levine, S., Terrell, D., et al. 2018, AAS Meeting Abstracts, **232**, 223.06
- Henry, T. J., Jao, W.-C., Winters, J. G., et al. 2018, *AJ*, **155**, 265
- Hippke, M., & Heller, R. 2019, *A&A*, **623**, A39
- Hord, B. J., Colón, K. D., Kostov, V., et al. 2021, *AJ*, **162**, 263
- Hord, B. J., Colón, K. D., Berger, T. A., et al. 2022, *AJ*, **164**, 13
- Howard, A. W., Marcy, G. W., Bryson, S. T., et al. 2012, *ApJS*, **201**, 15
- Howell, S. B., Everett, M. E., Sherry, W., Horch, E., & Ciardi, D. R. 2011, *AJ*, **142**, 19
- Hsu, D. C., Ford, E. B., & Terrien, R. 2020, *MNRAS*, **498**, 2249
- Huang, C., Wu, Y., & Triaud, A. H. M. J. 2016, *ApJ*, **825**, 98
- Huang, C. X., Vanderburg, A., Pál, A., et al. 2020a, *RNAAS*, **4**, 204
- Huang, C. X., Vanderburg, A., Pál, A., et al. 2020b, *RNAAS*, **4**, 206
- Huang, C. X., Quinn, S. N., Vanderburg, A., et al. 2020c, *ApJL*, **892**, L7
- Hubickyj, O., Bodenheimer, P., & Lissauer, J. J. 2005, *Icar*, **179**, 415
- Huehnerhoff, J., Ketzbeck, W., Bradley, A., et al. 2016, *Proc. SPIE*, **9908**, 99085H
- Hunter, J. D. 2007, *CSE*, **9**, 90
- Hwang, H.-C., Hamer, J. H., Zakamska, N. L., & Schlaufman, K. C. 2020, *MNRAS*, **497**, 2250
- Hwang, H.-C., Ting, Y.-S., & Zakamska, N. L. 2022, *MNRAS*, **512**, 3383
- Hwang, H.-C., & Zakamska, N. L. 2020, *MNRAS*, **493**, 2271
- Ida, S., & Lin, D. N. C. 2004, *ApJ*, **616**, 567
- Ida, S., & Lin, D. N. C. 2005, *ApJ*, **626**, 1045
- Ivanova, N., Justham, S., Chen, X., et al. 2013, *A&ARv*, **21**, 59
- Jackson, B., Greenberg, R., & Barnes, R. 2008, *ApJ*, **678**, 1396
- Jenkins, J. M., Caldwell, D. A., Chandrasekaran, H., et al. 2010, *ApJL*, **713**, L87
- Jenkins, J. M., Twicken, J. D., McCauliff, S., et al. 2016, *Proc. SPIE*, **9913**, 99133E
- Jensen-Clem, R., Duev, D. A., Riddle, R., et al. 2018, *AJ*, **155**, 32
- Johnson, D. R. H., & Soderblom, D. R. 1987, *AJ*, **93**, 864
- Johnson, J. A., Aller, K. M., Howard, A. W., & Crepp, J. R. 2010, *PASP*, **122**, 905
- Johnson, J. A., Gazak, J. Z., Apps, K., et al. 2012, *AJ*, **143**, 111
- Jordán, A., Hartman, J. D., Bayliss, D., et al. 2022, *AJ*, **163**, 125
- Kanodia, S., Cañas, C. I., Stefansson, G., et al. 2020, *ApJ*, **899**, 29
- Kanodia, S., Libby-Roberts, J., Canas, C. I., et al. 2022, arXiv:2203.07178
- Kanodia, S., Mahadevan, S., Ramsey, L. W., et al. 2018, *Proc. SPIE*, **10702**, 107026Q
- Kanodia, S., & Wright, J. 2018, *RNAAS*, **2**, 4
- Kaplan, K. F., Bender, C. F., Terrien, R. C., et al. 2019, in ASP Conf. Ser. 523, *Astronomical Data Analysis Software and Systems XXVII*, ed. P. J. Teuben et al. (San Francisco, CA: ASP), 567
- Kasper, D. H., Ellis, T. G., Yeigh, R. R., et al. 2016, *PASP*, **128**, 105005
- Kempton, E. M. R., Bean, J. L., Louie, D. R., et al. 2018, *PASP*, **130**, 114401
- Kennedy, G. M., & Kenyon, S. J. 2008, *ApJ*, **673**, 502
- Kervella, P., Arenou, F., Mignard, F., & Thévenin, F. 2019, *A&A*, **623**, A72
- Kiefer, F., Hébrard, G., Sahlmann, J., et al. 2019, *A&A*, **631**, A125
- Kipping, D. M. 2013a, *MNRAS*, **435**, 2152
- Kipping, D. M. 2013b, *MNRAS*, **434**, L51
- Kiseleva, L. G., Eggleton, P. P., & Mikkola, S. 1998, *MNRAS*, **300**, 292
- Knutson, H. A., Fulton, B. J., Montet, B. T., et al. 2014, *ApJ*, **785**, 126
- Kovács, G., Hodgkin, S., Sipőcz, B., et al. 2013, EPJC, **47**, 01002
- Kovács, G., Zucker, S., & Mazeh, T. 2002, *A&A*, **391**, 369
- Kreidberg, L. 2015, batman: BASIC Transit Model cAlculationN in Python, Astrophysics Source Code Library, ascl:1510.002
- Kunimoto, M., Daylan, T., Guerrero, N., et al. 2022, *ApJS*, **259**, 33
- Lainey, V. 2016, *CeMDA*, **126**, 145
- Lainey, V., Arlot, J., Karatekin, O., & Van Hoolst, T. 2009, AAS Meeting Abstracts, **41**, 66.01
- Lamman, C., Baranec, C., Berta-Thompson, Z. K., et al. 2020, *AJ*, **159**, 139
- Laughlin, G., Bodenheimer, P., & Adams, F. C. 2004, *ApJL*, **612**, L73
- Liang, M.-C., Seager, S., Parkinson, C. D., Lee, A. Y. T., & Yung, Y. L. 2004, *ApJL*, **605**, L61
- Lightcurve Collaboration, Cardoso, J. V. D. M. A., Hedges, C., et al. 2018, *Lightcurve: Kepler and TESS time series analysis in Python*, Astrophysics Source Code Library, ascl:1812.013
- Lin, D. N. C., Bodenheimer, P., & Richardson, D. C. 1996, *Natur*, **380**, 606
- Lindgren, L., Klioner, S. A., Hernández, J., et al. 2021, *A&A*, **649**, A2
- Line, M. R., Liang, M. C., & Yung, Y. L. 2010, *ApJ*, **717**, 496
- Maciejewski, G. 2020, *AcA*, **70**, 181
- Mahadevan, S., Ramsey, L., Bender, C., et al. 2012, *Proc. SPIE*, **8446**, 84461S
- Mahadevan, S., Ramsey, L. W., Terrien, R., et al. 2014, *Proc. SPIE*, **9147**, 91471G
- Maldonado, J., Micela, G., Baratella, M., et al. 2020, *A&A*, **644**, A68
- Manara, C. F., Morbidelli, A., & Guillot, T. 2018, *A&A*, **618**, L3
- Mandel, K., & Agol, E. 2002, *ApJL*, **580**, L171
- Mankovich, C. R., & Fuller, J. 2021, *NatAs*, **5**, 1103
- Marley, M. S., Ackerman, A. S., Cuzzi, J. N., & Kitzmann, D. 2013, in *Clouds and Hazes in Exoplanet Atmospheres*, ed. S. J. Mackwell et al. (Tucson, AZ: Univ. of Arizona Press), 367
- Martin, D. V., El-Badry, K., Hodžić, V. K., et al. 2021, *MNRAS*, **507**, 4132
- Marzari, F., & Thebault, P. 2019, *Galax*, **7**, 84
- Masci, F. J., Laher, R. R., Rusholme, B., et al. 2019, *PASP*, **131**, 018003
- Mayor, M., Marmier, M., Lovis, C., et al. 2011, arXiv:1109.2497
- McKinney, W. 2010, in *Proc. of the 9th Python in Science Conf.*, ed. S. van der Walt & J. Millman (Austin, TX: SciPy), 51
- Metcalf, A., Anderson, T., Bender, C., et al. 2019, *Optica*, **6**, 233
- Miller, N., & Fortney, J. J. 2011, *ApJL*, **736**, L29
- Mohanty, S., Greaves, J., Mortlock, D., et al. 2013, *ApJ*, **773**, 168
- Mordasini, C., Alibert, Y., Benz, W., Klahr, H., & Henning, T. 2012, *A&A*, **541**, A97
- Moses, J. I., Visscher, C., Fortney, J. J., et al. 2011, *ApJ*, **737**, 15
- Muirhead, P. S., Dressing, C. D., Mann, A. W., et al. 2018, *AJ*, **155**, 180
- Mulders, G. D., Pascucci, I., & Apai, D. 2015, *ApJ*, **798**, 112
- Mustill, A. J., Davies, M. B., & Johansen, A. 2015, *ApJ*, **808**, 14
- Naoz, S., Farr, W. M., Lithwick, Y., Rasio, F. A., & Teysandier, J. 2011, *Natur*, **473**, 187
- Neves, V., Bonfils, X., Santos, N. C., et al. 2013, *A&A*, **551**, A36
- Newton, E. R., Irwin, J., Charbonneau, D., et al. 2016, *ApJ*, **821**, 93
- Ngo, H., Knutson, H. A., Hinkley, S., et al. 2015, *ApJ*, **800**, 138
- Ngo, H., Knutson, H. A., Hinkley, S., et al. 2016, *ApJ*, **827**, 8
- Ninan, J. P., Bender, C. F., Mahadevan, S., et al. 2018, *Proc. SPIE*, **10709**, 107092U
- Nordhaus, J., & Spiegel, D. S. 2013, *MNRAS*, **432**, 500
- Nordhaus, J., Spiegel, D. S., Ibgui, L., Goodman, J., & Burrows, A. 2010, *MNRAS*, **408**, 631
- Obermeier, C., Koppenhoefer, J., Saglia, R. P., et al. 2016, *A&A*, **587**, A49
- Osborn, A., & Bayliss, D. 2020, *MNRAS*, **491**, 4481
- Paczynski, B. 1971, *ARA&A*, **9**, 183

- Paczynski, B. 1976, in *Structure and Evolution of Close Binary Systems*, ed. P. Eggleton, S. Mitton, & J. Whelan, Vol. 73 (Cambridge: Cambridge Univ. Press), 75
- Penoyre, Z., Belokurov, V., Wyn Evans, N., Everall, A., & Koposov, S. E. 2020, *MNRAS*, 495, 321
- Petigura, E. A., Marcy, G. W., Winn, J. N., et al. 2018, *AJ*, 155, 89
- Petrovich, C. 2015a, *ApJ*, 799, 27
- Petrovich, C. 2015b, *ApJ*, 805, 75
- Pineda, J. S., Youngblood, A., & France, K. 2021, *ApJ*, 911, 111
- Pollack, J. B., Hubickyj, O., Bodenheimer, P., et al. 1996, *Icar*, 124, 62
- Price-Whelan, A. M., Hogg, D. W., Foreman-Mackey, D., & Rix, H.-W. 2017, *ApJ*, 837, 20
- Ramsey, L. W., Adams, M. T., Barnes, T. G., et al. 1998, *Proc. SPIE*, 3352, 34
- Ramsey, L. W., Sebring, T. A., & Sneden, C. A. 1994, *Proc. SPIE*, 2199, 31
- Rasio, F. A., & Ford, E. B. 1996, *Sci*, 274, 954
- Reinhold, T., & Hekker, S. 2020, *A&A*, 635, A43
- Ricker, G. R., Winn, J. N., Vanderspek, R., et al. 2015, *JATIS*, 1, 014003
- Riello, M., De Angeli, F., Evans, D. W., et al. 2021, *A&A*, 649, A3
- Robertson, P., Anderson, T., Stefánsson, G., et al. 2019, *JATIS*, 5, 015003
- Sabotta, S., Schlecker, M., Chaturvedi, P., et al. 2021, *A&A*, 653, A114
- Schönrich, R., Binney, J., & Dehnen, W. 2010, *MNRAS*, 403, 1829
- Schwab, C., Rakich, A., Gong, Q., et al. 2016, *Proc. SPIE*, 9908, 99087H
- Scott, N. J., Howell, S. B., Horch, E. P., & Everett, M. E. 2018, *PASP*, 130, 054502
- Seager, S., & Mallén-Ornelas, G. 2003, *ApJ*, 585, 1038
- Shetrone, M., Cornell, M. E., Fowler, J. R., et al. 2007, *PASP*, 119, 556
- Sing, D. K. 2018, arXiv:1804.07357
- Sing, D. K., Fortney, J. J., Nikolov, N., et al. 2016, *Natur*, 529, 59
- Speagle, J. S. 2020, *MNRAS*, 493, 3132
- Stamatellos, D., & Herczeg, G. J. 2015, *MNRAS*, 449, 3432
- Stassun, K. G., Oelkers, R. J., Paegert, M., et al. 2019, *AJ*, 158, 138
- Stassun, K. G., & Torres, G. 2021, *ApJL*, 907, L33
- Stefánsson, G., Cañas, C., Wisniewski, J., et al. 2020, *AJ*, 159, 100
- Stefánsson, G., Hearty, F., Robertson, P., et al. 2016, *ApJ*, 833, 175
- Stefánsson, G., Mahadevan, S., Hebb, L., et al. 2017, *ApJ*, 848, 9
- Stefánsson, G., Mahadevan, S., Petrovich, C., et al. 2022, *ApJL*, 931, L15
- Steffen, J. H., Ragozzine, D., Fabrycky, D. C., et al. 2012, *PNAS*, 109, 7982
- Sudarsky, D., Burrows, A., & Hubeny, I. 2003, *ApJ*, 588, 1121
- Tenenbaum, P., & Jenkins, J. 2018, TESS Science Data Products Description Document, Technical Report 20180007935, <https://ntrs.nasa.gov/archive/nasa/casi.ntrs.nasa.gov/20180007935.pdf>
- Thorngren, D. P., & Fortney, J. J. 2018, *AJ*, 155, 214
- Thorngren, D. P., Fortney, J. J., Lopez, E. D., Berger, T. A., & Huber, D. 2021, *ApJL*, 909, L16
- Tokovinin, A. 2020, *MNRAS*, 496, 987
- Triaud, A. H. M. J. 2018, *Handbook of Exoplanets* (Berlin: Springer), 2
- Tuomi, M., Jones, H. R. A., Barnes, J. R., Anglada-Escudé, G., & Jenkins, J. S. 2014, *MNRAS*, 441, 1545
- Tuomi, M., Jones, H. R. A., Butler, R. P., et al. 2019, arXiv:1906.04644
- Van Cleve, J. E., Christiansen, J. L., Jenkins, J. M., et al. 2016, in *Kepler Science Document KSCI-19040-005*, ed. D. Caldwell
- van der Walt, S., Colbert, S. C., & Varoquaux, G. 2011, *CSE*, 13, 22
- van Roestel, J., Bellm, E. C., Duev, D. A., et al. 2019, *RNAAS*, 3, 136
- VanderPlas, J. T. 2018, *ApJS*, 236, 16
- Vick, M., Lai, D., & Anderson, K. R. 2019, *MNRAS*, 484, 5645
- Virtanen, P., Gommers, R., Oliphant, T. E., et al. 2020, *NatMe*, 17, 261
- Wahl, S. M., Hubbard, W. B., Militzer, B., et al. 2017, *GeoRL*, 44, 4649
- Wang, J., Fischer, D. A., Xie, J.-W., & Ciardi, D. R. 2014, *ApJ*, 791, 111
- Wang, X.-Y., Rice, M., Wang, S., et al. 2022, *ApJL*, 926, L8
- Wang, X.-Y., Wang, Y.-H., Wang, S., et al. 2021, *ApJS*, 255, 15
- Weidenschilling, S. J., & Marzari, F. 1996, *Natur*, 384, 619
- Winn, J. N. 2010, arXiv:1001.2010
- Winn, J. N., & Fabrycky, D. C. 2015, *ARA&A*, 53, 409
- Wright, E. L., Eisenhardt, P. R. M., Mainzer, A. K., et al. 2010, *AJ*, 140, 1868
- Wright, J. T., & Eastman, J. D. 2014, *PASP*, 126, 838
- Wright, J. T., Marcy, G. W., Howard, A. W., et al. 2012, *ApJ*, 753, 160
- Wu, Y., & Murray, N. 2003, *ApJ*, 589, 605
- Xiang, M. S., Liu, X. W., Yuan, H. B., et al. 2017, *MNRAS*, 467, 1890
- Yao, Y., Miller, A. A., Kulkarni, S. R., et al. 2019, *ApJ*, 886, 152
- Yee, S. W., Petigura, E. A., & von Braun, K. 2017, *ApJ*, 836, 77
- Yuan, H. B., Liu, X. W., Huo, Z. Y., et al. 2015, *MNRAS*, 448, 855
- Zechmeister, M., & Kürster, M. 2009, *A&A*, 496, 577
- Zechmeister, M., Reiners, A., Amado, P. J., et al. 2018, *A&A*, 609, A12
- Zhong, J., Lépine, S., Hou, J., et al. 2015, *AJ*, 150, 42
- Zhong, J., Li, J., Carlin, J. L., et al. 2019, *ApJS*, 244, 8
- Zhou, G., Huang, C. X., Bakos, G. Á, et al. 2019, *AJ*, 158, 141
- Zhu, W., Dai, F., & Masuda, K. 2018, *RNAAS*, 2, 160
- Zhu, W., & Dong, S. 2021, *ARA&A*, 59, 291